Perspective

Revisiting the Fundamentals of Photon-Assisted Reduction of Carbon Dioxide: Insights into the Interfacial Reactions and Electron Transfer Mechanism

Hariprasad Narayanan [1,2,*] , Harindranathan Nair [1] and Balasubramanian Viswanathan [2,*]

[1] School of Environmental Studies, Cochin University of Science and Technology, Cochin 682022
[2] National Centre for Catalysis Research, Department of Chemistry, Indian Institute of Technology Madras, Chennai 600036
* Correspondence: hariprasadmandur@gmail.com (H.N); bviswanathan@gmail.com (B.V)

Abstract: The scientific community has extensively studied photon-assisted carbon dioxide reduction for the past four decades as a crucial pathway in CO_2 conversion. However, the underlying mechanism of CO_2 reduction remains elusive, and the existing knowledge is inadequate for large-scale implementation due to the numerous obstacles associated with the reduction process. The reductive photon-assisted conversion of CO_2 encompasses a wide array of redox reactions at the semiconductor interface, including water splitting, oxygen evolution, hydrogen evolution, photo-oxidative reactions, and radical intermediate reactions, all of which significantly contribute to the overall product yield. This review seeks to elucidate the current understanding of interface reactions and their role in the fundamental mechanistic aspects of photon-assisted CO_2 conversion by identifying and analyzing the key factors involved.

1. The Intersection of CO_2 Conversion and Solar Technology

The rise in atmospheric carbon dioxide (CO_2) levels stems from the inefficient conversion of fossil carbon into useful energy and the excessive energy consumption by humans. Only around 32% of fossil carbon is transformed into valuable energy, while the remaining portion is discharged as heat into the atmosphere. This overexploitation of fossil fuels has led to the depletion of fossil fuel reserves and a corresponding surge in atmospheric CO_2 levels. Although there is some debate regarding the impact of CO_2 on climate change, reducing our reliance on fossil fuels is crucial to preserve natural resources and transition to renewable energy sources [1].

Human activities contribute approximately 38 Gt of anthropogenic-induced CO_2 to the atmosphere each year, surpassing nature's capacity to manage it. The natural carbon cycle processes about 800 Gt of CO_2 annually through photosynthesis; however, the additional CO_2 from human activities is too much for nature to handle. Consequently, it is essential to develop an artificial CO_2 cycle that can integrate with the natural carbon cycle and produce goods more selectively and at a higher rate.

The critical challenge for carbon capture and utilization technologies is to directly use CO_2 to produce industrial platform chemicals and fuels, which can limit the exploitation of fossil fuels to below their annual generation rate while preserving fossil carbon energy for future generations. As the energy demand continues to grow, it is essential to utilize alternative energy sources that reduce CO_2 emissions and minimize environmental impact.

Perennial energy sources and their derivatives have limited distribution potential and are unavailable 24/7, making them unsuitable for global transportation and consumption.

On the other hand, fossil carbon energy can be transported to and utilized at any location as required. Biomass, which includes organic materials like crops, wood, and waste, is commonly burned for energy, but this approach has several drawbacks. Burning biomass emits harmful chemicals and particulate matter, which adversely affects the environment and human health. Furthermore, using biomass as an energy source is not a comprehensive solution for reducing CO_2 emissions since burning is faster than its formation rate. Biomass requires additional processing and upgradation to become a more efficient energy source [2].

CO_2 applications are typically classified as either utilization or conversion applications. Conversion involves chemically transforming CO_2 into other products, whereas utilization includes conversion and other applications that use CO_2 as a technical fluid without chemical conversion. These applications include packaging, cleaning, fire suppression, water treatment, and well regeneration.

Three classes of CO_2 reactions can be distinguished based on their energetics and the status of the CO_2 molecule [3]. The first class of reactions involves incorporating the entire CO_2 molecule into chemicals like carbonates, polycarbonates, carbamates, and polyurethanes. These processes can be either exergonic or moderately endergonic, and the oxidation state of C remains at 4. The second class of reactions involves intermediate energy processes that form C-C bonds without hydrogen consumption, which reduces the oxidation state of C to 3. The third reaction class requires energy and hydrogen, which reduces the oxidation state of C until it reaches -4 in CH_4.

The available energy determines the selection of the appropriate CO_2 reaction class. Only specific reactions in the first class can be achieved in an energy frame that depends on fossil fuels. However, new reactions in the third class have become feasible with the increasing use of renewable energy. The strategic approach to CO_2 utilization as a resource rather than waste, which imitates natural processes, has gained popularity since 1989, and converting CO_2 and water into valuable products such as energy-rich hydrocarbons and oxygen using solar energy has become a significant scientific challenge for the future [4].

This study focuses on a higher-energy CO_2 conversion process that utilizes CO_2 as a carbon source for fuel production. However, producing fuels from CO_2 within a fossil-fuel energy framework is impractical because the required hydrogen would lead to more CO_2 emissions than what is being fixed. Assuming that H_2 is generated via the Water Gas Shift Reaction (WGSR) in the syngas production process, the conversion of n CO_2 into a C_nH_{2n+2} hydrocarbon would necessitate $(n+1)H_2$ and release $(n+1)$ CO_2. Since the fuel market is much larger than the chemicals market, using CO_2 as a carbon source for fuel production could have a significant impact.

The potential of using CO_2 as a carbon source for fuel production is significant since the fuel market is much larger than the chemical market. However, in an energy framework dependent on fossil fuels, producing fuels from CO_2 is impractical because the required hydrogen generates more CO_2 emissions than what is being fixed, and the emissions during the synthetic and separation processes make the process unfeasible. Nevertheless, a new paradigm involving photovoltaics is expected to emerge, allowing for large-scale industrial exploitation of the methanation reaction, which would facilitate the conversion of fossil CO_2 into fuels and bring us closer to a "Man-made C-Cycle." Direct atmospheric capture (DAC) technology and solar energy offer another approach to converting CO_2 into fuels, and although it imitates natural photosynthesis, it is more efficient and faster. Nonetheless, the process requires perennial sources of energy since the use of fossil fuels is not sustainable. The solar energy-based CO_2-to-fuels conversion process is more efficient than natural photosynthesis but is not yet economically competitive with fossil-C-based technologies. However, it can become cost-competitive in the medium term and can be optimized for selectivity and chain elongation to produce long-chain hydrocarbons. It is essential to avoid using fossil C in this process to achieve its intended purpose.[5]

The conventional method of chemo-catalysis and thermal processes to convert CO_2 into fuels can be replaced with a more promising alternative using PV technology in elec-

trolysis. However, hydrogen production via electrolysis must be safely and efficiently stored, as there is often a mismatch between hydrogen production and utilization. Despite this challenge, the Man-Made C-cycle approach can be a cost-effective and practical option for converting solar energy into fuel. This transition involves implementing proton-coupled electron transfer (PCET) in water as a reducing agent for CO_2. Using engineered semiconductors that couple n-p-type materials to avoid exciton collapse represents the future of CO_2 and water co-processing, with recent literature reporting light efficiencies of over 10%. While using water as a reductant presents energy and environmental advantages, the low efficiency of the carbon reduction reaction is still a challenge due to difficulties in the reaction mechanism.

This review explores the electron transfer mechanism and interfacial reactions, along with the author's opinions on material and experimental design to address this issue.

2. Clarifying the Difference between Photocatalytic and Photosynthetic Processes

It is crucial to emphasize the differentiation between photocatalytic and photosynthetic processes in the current context. Despite the clear distinction established in the literature, many reputable scientists in the field and prestigious journals have published works on CO_2 reduction, water splitting, and N_2 reduction as photocatalytic processes, which is technically incorrect. Ensuring accurate scientific terminology is used in all publications to avoid confusion and maintain scientific integrity is essential. Photocatalysis and photosynthesis are two different processes that involve the use of light to drive chemical reactions. Photocatalysis is a process in which a catalyst accelerates a chemical reaction under the influence of light. For example, titanium dioxide is a commonly used photocatalyst that can break down organic pollutants in water or air when exposed to UV light. In photocatalysis, the reaction is thermodynamically downhill, requiring energy input from light to occur. Photosynthesis, on the other hand, is a process in which plants and other organisms use light energy to convert carbon dioxide and water into glucose and oxygen. This process is thermodynamically uphill, requiring energy input to occur. There are two types of photosynthesis: type 1 and type 2. Type 1 photosynthesis involves the transfer of electrons from a donor molecule to an acceptor molecule, while type 2 photosynthesis involves the transfer of electrons from a donor molecule to an electrode.
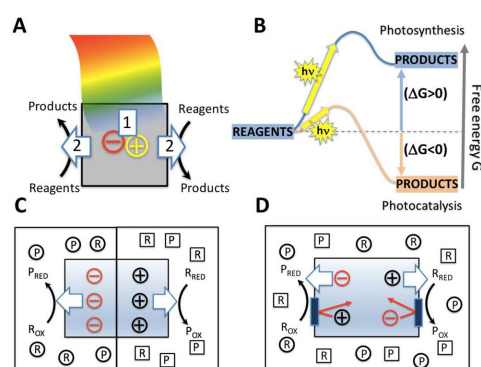
(a) Caption for figure 1

(b) Caption for figure 2

Figure 1. Overall caption for the two figures
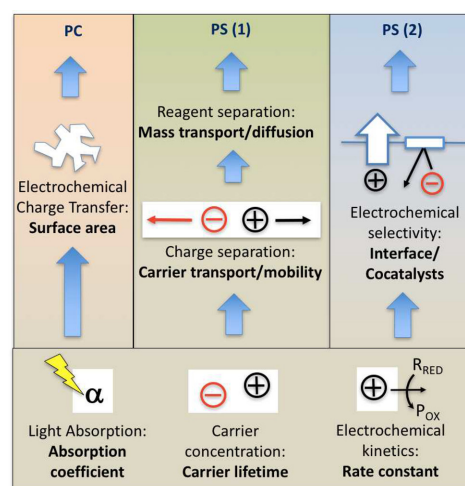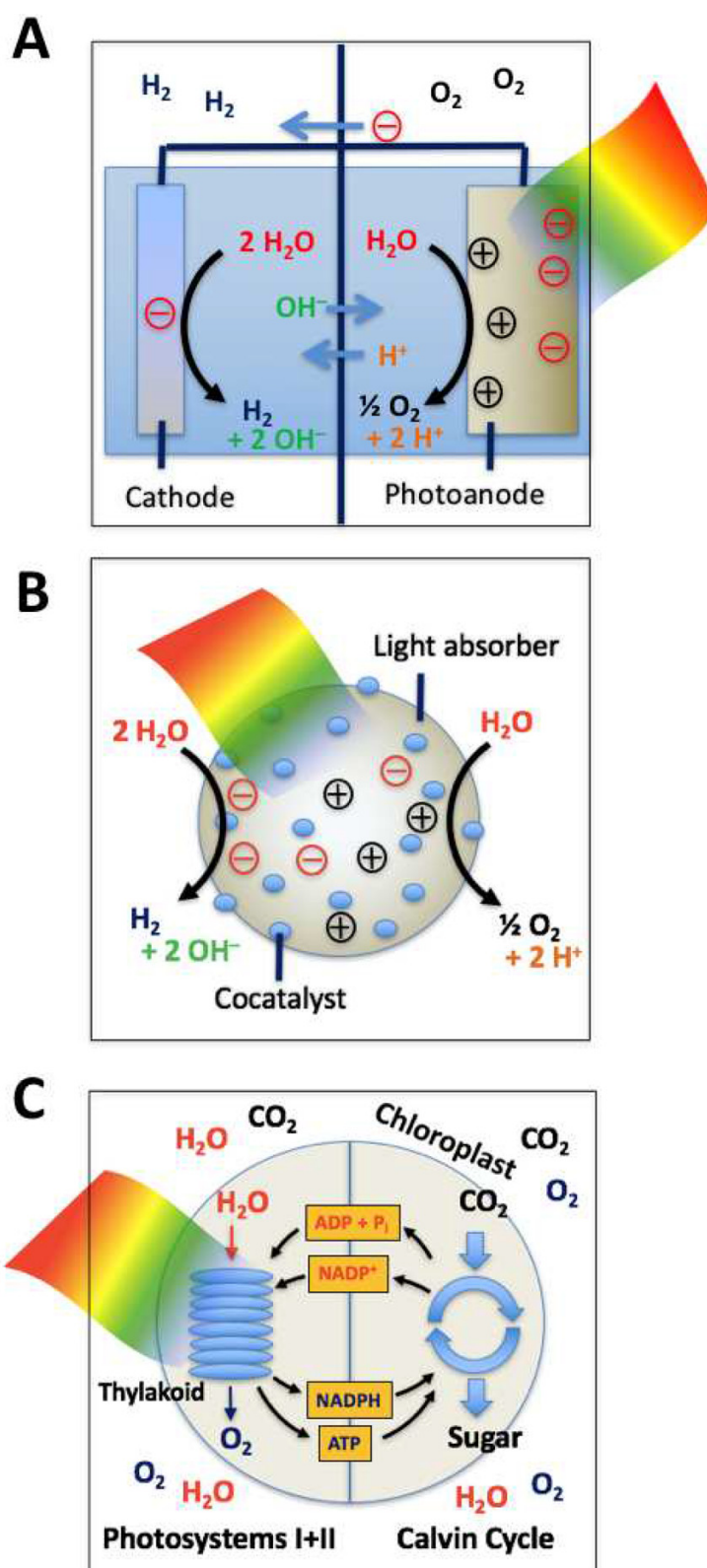
This is an example of a quote.

Figure 2. (A) Photoelectrochemical water-splitting cell (type 1 PS device). (B) Water-splitting photocatalysis as an example of a type 2 photosynthetic device. (C) Natural photosynthesis as example of a type 1/2 process with separate compartments for anodic and cathodic reactions and cocatalysts for selective photochemical charge transfer.

3. Fundamental Mechanisms of Carbon Dioxide Reduction via Electron Transfer

3.1. Single Electron Transfer

3.2. Multiple Proton Coupled Electron Transfer

4. Measures of efficiency

Various factors, including electron migration through band gap, electron transfer reactions, substrate adsorption, surface reactions, solvent medium, illumination source, reactor geometry, and other processes, influence the efficiency of photocatalysts in the carbon dioxide reduction process. Besides reducing carbon dioxide, conduction band electrons also participate in hydrogen production and superoxide formation. However, the overall efficiency of photocatalysts is determined by the sum of all the reactions, and the current efficiencies achieved are specific to certain reactions or sites. The current method of measuring efficiency is restricted to specific products and does not provide a comprehensive understanding of the actual efficiency of photocatalysts. Moreover, the absorbed light by the photocatalyst differs from that of the reaction medium, as light undergoes multiple reflections and scatterings before reaching the photocatalyst surface. Therefore, the efficiency measures used in photocatalysis should be revised to consider the overall reaction process and based on the photocatalyst and illumination, independent of individual parameters. This will enable the comparison of different photocatalyst systems and the selection of the most efficient one.

5. Product Analysis

The photocatalytic reduction of carbon dioxide results in the formation of a range of products in both liquid and gaseous states, including alcohols, acids, and aldehydes. It is crucial to accurately identify and quantify these products to determine the overall reaction efficiency and design better photocatalysts. Various analytical techniques such as GC, HPLC, LC-MS, IR, IEC, UV-Vis, and ^{1}H or ^{13}C NMR are commonly employed. However, due to the complexity of the multi-electron process, the oxidation of products and the formation of free radicals can create many by-products. Therefore, combining state-of-the-art techniques is necessary to identify and quantify products accurately.

Researchers have explored chromatographic techniques for analyzing CO_2 reduction products and proposed new methods for precise quantification with low detection limits. They also studied the impact of organic additives, such as sacrificial reagents and photo-sensitizers, on GC and HPLC analysis. It was found that alcohol analysis using GC is more sensitive to most organic additives, while HPLC acid and aldehyde analysis are primarily unaffected by the organic additives, except DMF and TEOA for formic and acetic acid, respectively

Improving the photocatalytic activity of CO_2 reduction through various preparative methods can lead to challenges in product analysis. These methods often involve organic solvents, high-temperature treatments, or vacuum annealing, which can introduce carbon impurities onto the photocatalyst surface. These impurities can affect the reaction, resulting in artificially elevated photoconversion rates. It is highly recommended to clean the surface before the reduction process to minimize the effect of such artefacts. If a sample contains 1% carbon residue per 0.1 grams of photocatalyst, the photoproduction rate after irradiation can be much higher than many reported values

A systematic assay of products is essential for an accurate evaluation of photoactivity in advanced photocatalyst designs. Combining $^{13}CO_2$ tracer experiments can address these issues and is best analyzed using ^{13}C NMR or GCMS. However, before conducting isotopically labelled experiments, it is crucial to ensure the purity of the isotope used, as low-grade samples of $^{13}CO_2$ may contain trace amounts of $^{13}CH_4$. The purity of the isotope must be confirmed to avoid obtaining contaminated results. Yang et al. studied the undesired role of carbon artefacts through FTIR measurements using isotopically labelled CO_2.
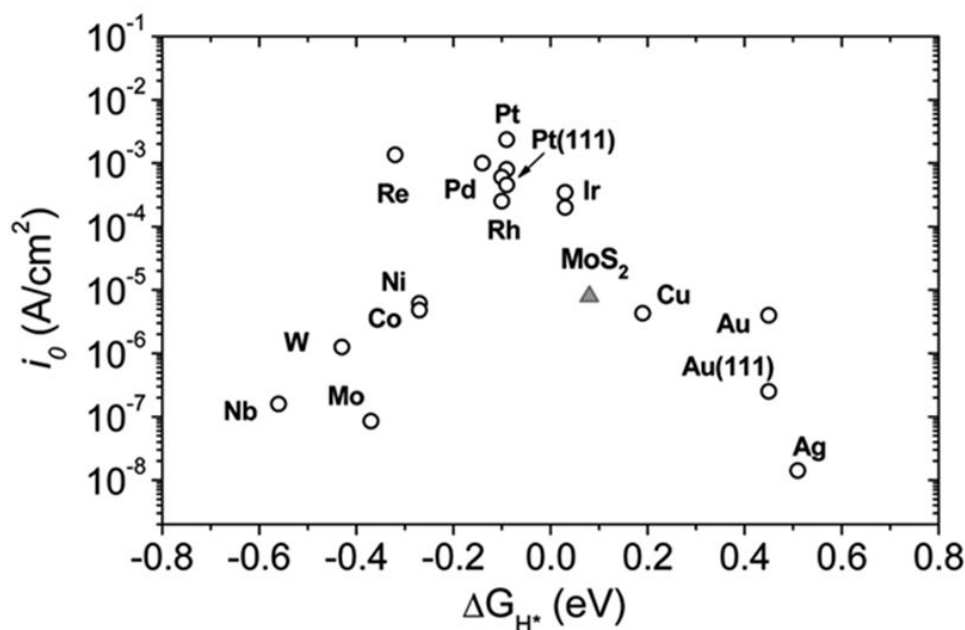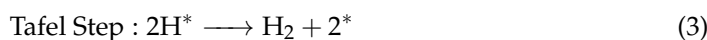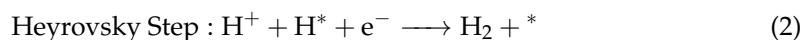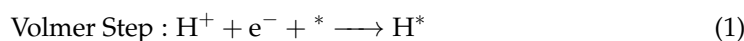
Figure 3. HER volcano curve of MoS_2 vs. metals. (Reproduced with permission from J.K. Nørskov, T. Bligaard, A. Logadottir, J.R. Kitchin, J.G. Chen, S. Pandelov, U. Stimming, Trends in the exchange current for hydrogen evolution, J. Electrochem. Soc. 152 (2005) J23–J26. ©2005 by ECS-The Electrochemical Society.)

6. The Interface Challenge: Competing Chemical Reactions in CO_2 Reduction

6.1. Hydrogen Evolution Reaction

The effectiveness of a photoelectrode in producing hydrogen is largely determined by the availability of active sites on its surface. Even if a photoelectrode has the desired band-edge positions and generates adequate photovoltage, it cannot produce a substantial amount of hydrogen if its surface is inactive. The hydrogen evolution process on a catalyst surface can follow two mechanisms: the Volmer-Heyrovsky or the Volmer-Tafel mechanism [269–271].
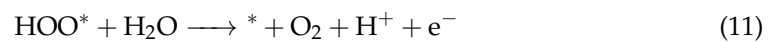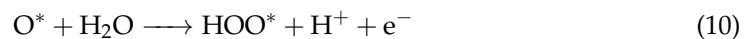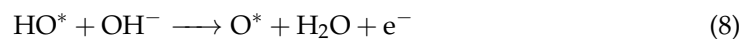
$$\text{Volmer Step}: H^+ + e^- + {}^* \longrightarrow H^* \tag{1}$$

$$\text{Heyrovsky Step}: H^+ + H^* + e^- \longrightarrow H_2 + {}^* \tag{2}$$

$$\text{Tafel Step}: 2H^* \longrightarrow H_2 + 2^* \tag{3}$$

To efficiently produce hydrogen, a photoelectrode should possess surface active sites that bind reaction intermediates not too weakly nor too firmly, following the Sabatier principle. If the adsorption is too weak, the overall reaction rate is limited by the Volmer step, whereas if it's too strong, the reaction rate is limited by the desorption of intermediates from the surface, either through Heyrovsky or Tafel step. Thus, an active catalyst towards hydrogen evolution must satisfy the condition of $\Delta G_{H^*} \approx 0$, which is insufficient but necessary [272,273]. Empirical studies show a volcano-type relationship between experimentally determined current density and ΔG_H of various catalyst materials [274-276].

Designing an effective catalyst material requires controlling the binding energies of active intermediate species to the active surface sites. While volcano plots provide insight into catalyst design for HER, a quantitative measurement of absolute reaction rate is necessary for each class of materials. This is because the kinetic barrier associated with a process varies depending on the material used and the pH of the electrolyte [278]. Interestingly, the catalytic activity in the volcano curve changes up and down with pH or kinetic barrier, not in the left-right direction, indicating the applicability of the descriptor in designing material for HER under any conditions [279].

Platinum is currently the best catalyst material for HER as it only needs a negligible overpotential in acidic conditions [269], however, its high cost and low abundance limits its use. Researchers have turned to exploring new earth-abundant materials and have found that MoS_2 edge sites possess $\Delta G_H \approx 0.08 eV$ at 50% hydrogen coverage, close to the thermoneutral ΔG_H value [280]. Studies on MoS_2 have reported that the hydrogen evolution activity depends on the perimeter length of the edge site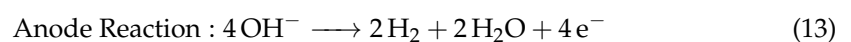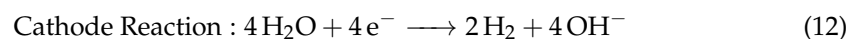s rather than the increased surface area [277]. A three-dimensional porous structure with double-gyroid morphology can marginally increase the turnover frequency of MoS_2, but the longer transport distance to the active sites can cause resistance to electron flow, so lower-dimensional materials are preferable for vectorial electron transfer reactions such as water splitting [282]. Although there have been remarkable studies to increase the active edge sites on the MoS_2 surface, the overall activity of the electrode is still limited due to the small fraction of the edge sites responsible for the reaction rate. This led researchers to explore other catalyst systems with higher intrinsic activity, such as metal nitrides [283], carbides [284,285], borides [284], phosphides [286,287], and selenides [288]. These systems exhibit higher HER activity closer to that of Pt in terms of the overpotential required to reach a current density of $10\ mA\ cm^{-2}$. However, the higher catalyst loading and surface area limit the non-precious catalyst system orders of magnitude behind Pt when considering the TOF_{avg} under acidic conditions. In basic conditions, the Ni-Mo [289] system shows a lower overpotential to reach $10\ mA\ cm^{-2}$ but has substantially lower TOF than Pt. Developing a catalyst system for HER reaction requires significant effort and remains a critical challenge. The design of a catalyst system should take into account its long-term stability, which is equally important as activity for any technologically viable reactions.

6.2. Oxygen Evolution Reaction

The process of oxygen evolution reaction (OER) is crucial for the PEC water splitting process, but it is known to have slower kinetics due to the transfer of four excitons. The main intermediates observed in the OER process are O^*, HO^* and HOO^* [269]. The stability of these intermediates on the surface is highly influenced by the M-O bonding interaction, which in turn affects the efficiency of water splitting. In an acidic medium, the OER reaction mechanism can be described by the following equation [290]:

$$\text{Cathode Reaction}: 4\,H^+ + 4\,e^- \longrightarrow 2\,H_2 \tag{4}$$

$$\text{Anode Reaction}: 2\,H_2O \longrightarrow O_2 + 4\,H^+ + 4\,e^- \tag{5}$$

$$\text{Overall Reaction}: 2\,H_2O \longrightarrow 2\,H_2 + O_2 \tag{6}$$

$$^* + H_2O \longrightarrow HO^* + H^+ + e^- \tag{7}$$

$$HO^* + OH^- \longrightarrow O^* + H_2O + e^- \tag{8}$$

$$2\,O^* \longrightarrow 2\,^* + O_2 \tag{9}$$

$$O^* + H_2O \longrightarrow HOO^* + H^+ + e^- \tag{10}$$

$$HOO^* + H_2O \longrightarrow\ ^* + O_2 + H^+ + e^- \tag{11}$$

In akaline medium,

$$\text{Cathode Reaction}: 4\,H_2O + 4\,e^- \longrightarrow 2\,H_2 + 4\,OH^- \tag{12}$$

$$\text{Anode Reaction}: 4\,OH^- \longrightarrow 2\,H_2 + 2\,H_2O + 4\,e^- \tag{13}$$

$$OH^- +\ ^* \longrightarrow HO^* \tag{14}$$

$$HO^* + OH^- \longrightarrow O^* + H_2O \tag{15}$$

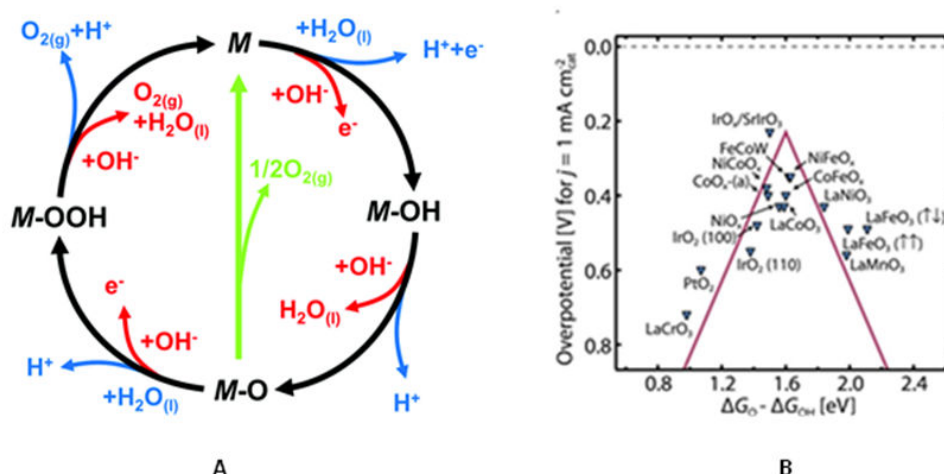$$2\,O^* \longrightarrow 2\,^* + O_2 \tag{16}$$
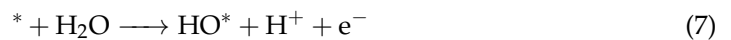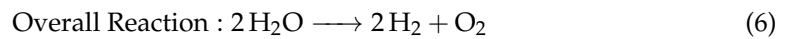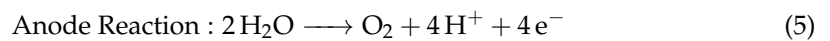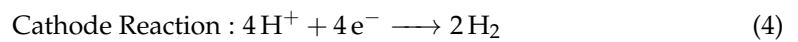
Figure 4. (A) OER mechanism in acid (blue lines—gray in print version) as well as in alkaline medium (red lines—dark gray in print version). (B) Activity trends toward OER on metal oxides. ((A) Reproduced with permission from N.-T. Suen, S.-F. Hung, Q. Quan, N. Zhang, Y.-J. Xu, H.M. Chen, Electrocatalysis for the oxygen evolution reaction: recent development and future perspectives, Chem. Soc. Rev. 46 (2017) 337–365. ©2017 The Royal Society of Chemistry. (B) Reproduced with permission from Isabela C. Man, Hai-Yan Su, Federico Calle-Vallejo, Heine A. Hansen, Jose I. Martínez, Nilay G. Inoglu, John Kitchin, Thomas F. Jaramillo, Jens K. Nørskov, Jan Rossmeisl, Universality in oxygen evolution electrocatalysis on oxide surfaces, ChemCatChem 3 (2011) 1159–1165. ©2011 John Wiley & Sons, Inc.)

$$O^* + OH^- \longrightarrow HOO^* + e^- \tag{17}$$

$$HOO^* + HO^- \longrightarrow {}^* + O_2 + H_2O \tag{18}$$
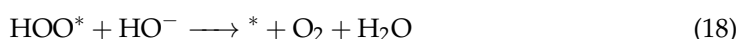
Metal oxide catalysts, including perovskites, RuO_2, IrO_2, $IrO_x/SrIrO_3$, Ni-oxides, Co-oxides, Mn-oxides, and tertiary oxyhydroxides, are commonly used as electrocatalysts for the OER [290]. Similarly to the HER, a volcano-type relationship can be observed in the OER using the ($\Delta G^\circ_{OER} - \Delta G^\circ_H$) descriptor [291]. The fundamental overpotential of the reaction can be minimized by stabilizing the HOO^* intermediate with respect to the HO^* intermediate on the catalyst surface.

6.3. Sacrificial Reagent and Reactive Oxygen Species

The primary advantage of photocatalysts is the availability of redox sites on the same surface. However, this benefit can also be a disadvantage in many cases, as described in various literature reviews on the role of sacrificial reagents in photocatalytic reactions. Adding sacrificial reagents into the reaction system complicates the reduction process and absorbs irradiated light. Using sacrificial reagents in chemical production can be uneconomical, as they initially increase product yield but eventually disintegrate into various products. Common sacrificial reagents include organic electron donors such as methanol, organic acids, and hydrocarbons, which are also the main reduction products of CO_2 reduction. Therefore, using these sacrificial agents in the CO_2 reduction process is not feasible.

Inorganic electron donors, such as sulfide (S^{2-}) and sulfite (SO_3^{2-}), serve as sacrificial reagents. These donors primarily capture the hole from the valence band and transform it into corresponding ions.

Many current studies have focused on direct hole oxidation reactions, while inorganic electron donors can undergo a series of electron-coupled proton transfer reactions within the potential range of CO_2 reduction.

Adding carbonate or bicarbonate ions enhances the stoichiometric hydrogen and oxygen evolution from water, suppressing the backward reaction of H_2 and O_2 to water over deposited metallic surfaces and promoting water splitting into H_2 and O_2. Surprisingly, despite their well-established nature, many current articles do not consider these possibilities in the case of aqueous phase CO_2 reduction. Direct hole oxidation of HCO_3^-/CO_3^{2-} is thermodynamically more feasible than proton-coupled electron reduction. In aqueous phase reduction, CO_2 precursors increase the rate of competing hydrogen and oxygen evolution reactions

Recent studies have demonstrated that carbonate ions in a solution significantly increase water-splitting reactions on metal-supported photocatalysts, such as TiO_2. In-depth investigations on the effect of carbonate on hydrogen evolution reveal that this effect is more pronounced in TiO_2 than in other materials. Based on the impact of carbonate addition, photocatalysts can be classified into four groups.

Based on the effect of carbonate addition, photocatalysts can be classified into four groups:

1. Photocatalysts that can split water only in the presence of carbonates: Pt/TiO_2, $RuO2/TiO_2$, $NiOx/TiO_2$, Rh/TiO_2, Cu/TiO_2, Pt/ZrO_2, Pt/K_4Nb_6O7, $Pt/K_2Ti_6O_{13}$, and $Pr/Na_2Ti_6O_{13}$
2. Photocatalysts whose activity is enhanced by the addition of carbonates: RuO_5/Ta_2O_5, $Rh/SrTiO_3$, $NiOx/SrTiO_3$, $RuO_2/Na_2Ti_6O_{13}$, $RuO_2/K_2Ti_6O_{13}$, and $RuO_2/BaTi_4O_6$
3. Photocatalysts whose activities remain unchanged with the addition of carbonates: RuO_2/ZrO_2 and $Pt/SrTiO_3$
4. Photocatalysts whose activities decrease by the addition of carbonate ions: $NaTaO_3$, $LiTaO_3$, $KTaO_3$, $Ba_2Ta_2O_6$, $Sr_2Ta_2O_6$, $Sr_2Ta_2O_7$, and $Sr_2Nb_2O_7$

Reactive oxygen species (ROS) are crucial in photocatalytic CO_2 reduction. The in situ oxygen generated through water oxidation captures an electron from the conduction band and transforms it into a superoxide radical with higher oxidation potential. The products formed during the CO_2 reduction process are highly susceptible to the oxidative attack of ROS, and the oxidation of hydrocarbons produces CO_2 back into the reaction system. There is a chance for the carbon atom to undergo multiple reduction reactions cyclically. The main challenge is controlling the activity of in situ-produced oxygen and reactive oxygen species in the reaction system. Detailed information on the production and reactions of reactive oxygen species can be found in Table 4 of reference.

Hydroxyl radicals produced in the system react with carbonate species and form carbonate anion radicals. These carbonate anion radicals undergo a series of reactions with other inorganic radicals in the system. The hydroxyl radical is highly reactive, and its primary reaction mechanisms with organic compounds involve OH-addition, H-abstraction, and, to a lesser extent, electron-transfer reactions. The complex chemistry of these reactions, including radical kinetics and overall reaction pathways, plays a significant role in the behaviour of the system. Detailed information on the reactions of hydroxyl radicals and carbonate anion radicals can be found in Table 5 of reference.

Photo-oxidation of methanol is proposed to be carried out through two mechanisms: (1) direct hole oxidation and (2) oxidation by hydroxyl (OH) radicals formed by the oxidation of surface-adsorbed water. The hydroxyl radical oxidizes methanol if water is the predominant species at the surface, and in all other cases, direct hole oxidation is preferred. Methoxy and formate/formyl species play a vital role in the reaction, with methoxy species formed by thermal and photochemical dissociation of methanol. The formation of methyl formate is favoured by a high surface coverage of methoxy species, and surface and bridged oxygen atoms are also essential actors. Methanol concentration, among other reaction parameters, dramatically influences the selectivity of photooxidation.

The exact mechanism applies to all alcohols containing a hydrogen-bearing hydroxyl group attached to the alpha carbon atom. Similarly, the formate ion exhibits a similar mechanism, producing $CO_2^{\bullet-}$ as the reducing intermediate, believed to be the main intermediate product of CO_2 reduction. This type of reaction favours the formate-based CO_2

reduction mechanism. According to this mechanism, CO_2 is directly hydrogenated by a hydrogen atom produced due to a water-splitting process, forming an HCOO species that may undergo further protonation or C-O bond cleavage. The ESR-detected $CO_2^{\bullet-}$ on the surface of the photocatalyst may be produced directly from the adsorbed formate rather than the first electron addition to the CO_2 molecule.

The current doubling effect is observed in photoelectrochemical cells when an organic or inorganic sacrificial agent is added to the electrolyte, resulting in photocurrent multiplication. This effect occurs due to the formation of unstable radicals followed by electron injection into the conduction band of a photocatalyst in a photoelectrochemical cell functioning in the presence of sacrificial agents. In the current doubling effect, for one photon absorbed, one electron is photogenerated, and one is injected by the radical, resulting in two electrons being produced for one photon absorbed. This effect has been extensively studied and can have implications for the efficiency and performance of photoelectrochemical systems.

The role of the Nafion layer in the photosynthetic conversion of CO_2 to hydrocarbons on Pd/TiO_2 is to enhance the local proton activity within the layer to facilitate proton-coupled electron transfer (PCET) reactions, stabilize intermediates, and inhibit the re-oxidation of CO_2 reduction products. $Nf/Pd–TiO_2$ is more active than $Pd–TiO_2$ for the photoproduction of hydrocarbons, and its photosynthetic activity is maintained through repeated cycles of photoreaction, confirming the stability of the Nafion layer. The proposed $Nf/Pd–TiO_2$ catalyst is a model for more efficient catalysts for artificial photosynthesis. However, the photoconversion efficiency of the process is low because the activation of stable CO_2 requires highly energetic electrons. A conceptual analysis and possible adaptations for CO_2 reduction include:

1. Using a direct proton source other than water to facilitate CO_2 reduction. This could potentially increase the reactivity of the proton source and improve the efficiency of the process.
2. Employing a proton source that does not undergo any electrochemical reaction within the potential range for the CO_2 reduction reaction. This would ensure that the proton source remains stable and available for reduction.
3. Ensuring that the reactivity of the proton source is as high as that in Nafion, where the proton is in a highly electronegative environment of fluorine atoms. This would enhance the efficiency of the CO_2 reduction process.
4. Making available protons capable of reacting with CO_2 directly, promoted by the light absorbed in TiO2, and carrying out the reduction reaction on reactive metal sites. This would improve the overall efficiency of the process.
5. Overcoming the low solubility of CO_2 by using a carbonate source that can generate CO_2 in situ, sustaining the source for the reduction process. This would ensure a continuous supply of CO_2 for the reduction reaction, potentially improving the efficiency and feasibility of the process.

Considering the aspects mentioned earlier, it is possible that other proton-coupled electron transfer (PCET) catalyst support systems, which may sustain more acidic protons, can be tried, such as hetero-poly acids or superacids like sulfated zirconia. These alternative support systems could potentially enhance the efficiency and selectivity of CO_2 reduction reactions by providing a more acidic environment for the protons, similar to the highly electronegative environment of fluorine atoms in Nafion. By exploring these alternative catalyst support systems, researchers may develop more efficient and sustainable methods for CO_2 reduction, contributing to the advancement of artificial photosynthesis and carbon capture and utilization technologies.

6.3.1. Subsubsection

7. Photo-physics and Photo-chemistry of the Semiconductor Surface and Interface

In this section, we trace the path of charge carriers as they move toward the interfacial region of the semiconductor, beginning with an overview of the fundamental principles of

semiconductor physics and the semiconductor/electrolyte interface under both illuminated and non-illuminated conditions. This exploration delves into the behaviour of electrons and holes within semiconductors, their interactions with electrolytes, and the impact of light exposure on these processes. Understanding these core concepts is essential for advancing the field of photoelectrochemical energy conversion and optimizing the efficiency of solar fuel generation systems.

7.1. Semiconductor in Equilibrium

A comprehensive understanding of a system under equilibrium is crucial for enhancing our knowledge of energy conversion processes. This section examines the semiconductor without external influences such as electric fields, magnetic fields, voltage, and irradiation. Under equilibrium conditions, the properties of semiconductors remain time-independent. We begin by discussing intrinsic semiconductors and then move on to extrinsic ones commonly used as materials in semiconductor-based photon-assisted CO2 reduction systems. This analysis provides valuable insights into the behaviour of semiconductors and their role in energy conversion and environmental applications.

7.1.1. Charge Carries in Semiconductors

A semiconductor's characteristics depend on the distribution of charge carriers, such as electrons in the conduction band and holes in the valence band. The overall density of electrons and holes in a semiconductor is closely tied to the density of states and Fermi distribution functions. By considering the product of allowed quantum states and the probability of an electron occupying a state, we can determine the distribution of electrons in the conduction band, as illustrated in the following equation.

$$n(E) = g_c(E)f_F(E) \tag{19}$$

The equation for the distribution of electrons in the conduction band involves the density of quantum states in the conduction band, denoted as g_C, and the Fermi-Dirac probability function, f_F [8, 10]. The integration of Equation 19 yields the total concentration of electrons in the conduction band. Likewise, the distribution of holes in the valence band of the semiconductor can be expressed similarly as follows:

$$p(E) = g_V(E)[1 - f_F(E)] \tag{20}$$

In this equation, the distribution of holes in the valence band is determined by the product of the allowed quantum states in the valence band and the probability of that state not being occupied by an electron. The integration of Equation 20 yields the total concentration of holes in the valence band [8, 10].

Determining the positions of the Fermi energy (E_F) concerning the conduction band minimum (E_C) and valence band maximum (E_V) is crucial for determining the concentrations of electrons and holes in a semiconductor. The Fermi energy refers to the electrochemical potential of the electron, and under equilibrium conditions, it is assumed that the occupancy of the Fermi level is 50%. In intrinsic semiconductors, the valence band is filled with electrons at absolute temperature (T= 0 K), and hence, the Fermi level is situated at the mid-point of the bandgap when the effective masses of the electron and holes are equal.

As the temperature increases, more electrons occupy the conduction band, leaving holes in the valence band behind. The creation of a hole occurs when an electron from an adjacent covalent bond forms a bond with the electron vacancy. This continuous process enables the holes to move throughout the semiconductor. The concentration of electrons and holes is equal in intrinsic semiconductors with high purity and no lattice defects.

As previously mentioned, the equilibrium concentrations of electrons (n_0) and holes (p_0) can be determined by integrating Eq. 1 and Eq. 2, respectively, within the limits of E_C to ∞ and $-\infty$ to E_V, respectively [8-11].

$$n_0 = \int_{E_C}^{\infty} g_C(E) f_F(E) dE \tag{21}$$

Similarly,

$$p_0 = \int_{-\infty}^{E_V} g_V(E)[1 - f_F(E)] dE \tag{22}$$

The thermal equilibrium concentration of electrons and holes can be obtained by solving equation 21 and 22, respectively.

$$n_0 = N_C \exp\left[\frac{-(E_C - E_F)}{kT}\right] \tag{23}$$

$$p_0 = N_V \exp\left[\frac{-(E_F - E_V)}{kT}\right] \tag{24}$$

The effective density of states of the conduction and valence bands in a semiconductor material is denoted by N_C and N_V, respectively. These values remain constant for a given temperature and material. The Boltzmann constant, denoted by k, relates temperature to energy, and a slight temperature change can result in a significant increase in charge carrier concentration, as evidenced by the exponential relationship between carrier concentration and temperature.

$$N_C = 2\left(\frac{2\pi m_n^* kT}{h^2}\right)^{\frac{3}{2}} \tag{25}$$

$$N_V = 2\left(\frac{2\pi m_p^* kT}{h^2}\right)^{\frac{3}{2}} \tag{26}$$

The effective masses of electrons and holes in the semiconductor lattice are denoted by m_n^* and m_p^*, respectively. In the case of an intrinsic semiconductor, the carrier concentrations are equal, leading to $n_i = n_0 = p_i = p_0$. By multiplying Equation 23 and Equation 24 together, the carrier concentration of an intrinsic semiconductor can be calculated.

$$n_i{}^2 = N_C N_V \exp\left[\frac{-(E_C - E_V)}{kT}\right] = N_C N_V \exp\left[\frac{-E_g}{kT}\right] \tag{27}$$

E_g denotes the energy of the bandgap in this equation. This relationship shows that the carrier concentration of an intrinsic semiconductor remains constant at a given temperature, regardless of the position of the Fermi level. The position of the Fermi level in an intrinsic semiconductor can be easily determined using Equation 23 and Equation 24.

$$N_C \exp\left[\frac{-(E_C - E_{Fi})}{kT}\right] = N_V \exp\left[\frac{-(E_{Fi} - E_V)}{kT}\right] \tag{28}$$

To determine the position of the Fermi level in an intrinsic semiconductor, the equation above can be solved by taking the logarithm of both sides of the equation.

$$E_{Fi} = \frac{1}{2}(E_C + E_V) + \frac{1}{2}kT \ln\left(\frac{N_V}{N_C}\right) \tag{29}$$

By applying the definitions of N_V and N_C in Equation 27, the equation for the Fermi level can be redefined in terms of the effective masses of electrons and holes.

$$E_{Fi} = E_{midgap} + \frac{3}{4}kT \ln\left(\frac{m_p^*}{m_n^*}\right) \tag{30}$$

$$E_{Fi} - E_{midgap} = \frac{3}{4}kT \ln\left(\frac{m_p^*}{m_n^*}\right) \tag{31}$$
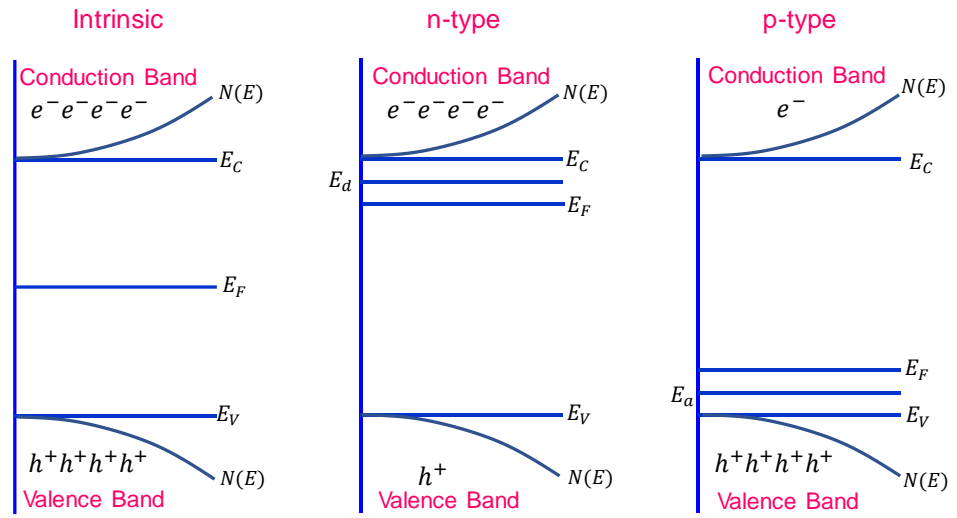
Figure 5. Representation of semiconductors at thermal equilibrium. (a) intrinsic (b) ntype and (c) p-type semiconductor.

Equation 31 reveals that the relative position of the Fermi level in an intrinsic semiconductor depends on the charge carriers effective masses, which are directly related to the density of states. If the effective masses of the carriers were equal, the Fermi level would be situated at the centre of the bandgap. In an n-type semiconductor, the majority of carriers are electrons, and the effective mass of electrons is greater than that of holes. Consequently, the Fermi level lies above the intrinsic Fermi level, such that $E_F > E_{Fi}$. Conversely, in a p-type semiconductor, the majority of carriers are holes, and the effective mass of holes is greater than that of electrons. Therefore, the Fermi level is situated below the intrinsic Fermi level, such that $E_F < E_{Fi}$ (see Figure 1).

In an n-type semiconductor, impurities can create an additional donor energy level, denoted by E_d, near the conduction band minimum. The energy required to excite an electron from the donor level to the conduction band is minimal compared to the energy required for bandgap excitation. Exciting electrons from the donor level produces positively charged species at the donor sites. These impurity atoms are typically referred to as donor impurity atoms, and they generate electrons in the conduction band without creating holes in the valence band. Conversely, in a p-type semiconductor, additional impurity atoms create an energy level near the valence band. A small amount of thermal energy is required to excite the valence electrons into the acceptor energy level, denoted by E_a. The electrons present in the acceptor energy level do not have sufficient energy to behave like conduction band electrons. The electrons fill the unoccupied orbitals of the acceptor impurity atoms, causing the impurity atom to become a negatively charged species fixed in the crystal, generating holes in the valence band without producing electrons in the conduction band. Extrinsic semiconductors can be formed from intrinsic semiconductors by adding small amounts of donor or acceptor impurity atoms.

For an n-type semiconductor, Eq.5 can be rewritten as [8-11],

$$n_0 = N_C \, exp \left[\frac{-(E_C - E_{Fi}) + (E_F - E_{Fi})}{kT} \right] \tag{32}$$

$$n_0 = N_C \exp \left[\frac{-(E_C - E_{Fi})}{kT} \right] \exp \left[\frac{(E_F - E_{Fi})}{kT} \right] \tag{33}$$

It is apparent from Equations 23 and 26 that,

$$n_i = N_C \exp\left[\frac{-(E_C - E_{Fi})}{kT}\right] \tag{34}$$

By substituting the value of "n_i" in Equation 15,

$$n_0 = n_i exp\left[\frac{(E_F - E_{Fi})}{kT}\right] \tag{35}$$

Likewise, we can express,

$$p_0 = p_i \exp\left[\frac{(E_F - E_{Fi})}{kT}\right] \tag{36}$$

The product of "n_0" and "p_0" in an extrinsic semiconductor is similar to the expression of the intrinsic semiconductor described earlier in Equation 25. In thermal equilibrium, as in previous cases, the product of the concentration of charge carriers is always constant at a specific temperature.

$$n_0 p_0 = n_i^2 \tag{37}$$

While appearing simple, the equation is a fundamental principle in semiconductor physics at thermal equilibrium and is derived using the Boltzmann approximation. However, if the approximation is invalid, the equilibrium concentration of electrons and holes can be expressed in terms of the Fermi-Dirac integral. [8-11]

$$n_o = \frac{4\pi}{h^2}(2m_n^* kT)^{\frac{3}{2}} \int_0^\infty \frac{\eta^{\frac{1}{2}} d\eta}{1 + \exp(\eta - \eta_F)}. \tag{38}$$

$$p_o = \frac{4\pi}{h^2}\left(2m_p^* kT\right)^{\frac{3}{2}} \int_0^\infty \frac{\eta'^{\frac{1}{2}} d\eta'}{1 + \exp(\eta' - \eta_F')} \tag{39}$$

The above equation involves the Fermi-Dirac integral, an integral function that plays a crucial role in semiconductor physics at thermal equilibrium. In the equation, η_F is defined as $\left[\frac{(E_F - E_C)}{kT}\right]$, η_F' as $\left[\frac{(E_V - E_F)}{kT}\right]$, η as $\left[\frac{(E - E_C)}{kT}\right]$, and η' as $\left[\frac{(E_V - E)}{kT}\right]$. It is worth noting that if $\eta_F > 0$ or $\eta_F' > 0$, the Fermi level would be located in the conduction band or valence band, respectively. Semiconductors with such properties are called degenerate semiconductors.

The degeneracy factor, which is related to the probability density of electrons and holes in the donor and acceptor levels, is described by the Pauli exclusion principle as [8-11],

$$n_d = \frac{N_d}{1 + \frac{1}{g}\exp\left(\frac{E_d - E_F}{kT}\right)} \tag{40}$$

$$p_a = \frac{N_a}{1 + \frac{1}{g}\exp\left(\frac{E_F - E_a}{kT}\right)} \tag{41}$$

The degeneracy factor g is related to the probability density of electrons and holes in the donor and acceptor level. The equations can be represented in a more straightforward form as $n_d = N_d - N_d^+$ and $p_a = N_a - N_a^+$. In materials with donor or acceptor levels, such as n-type or p-type semiconductors, at room temperature, electrons and holes are present in the conduction and valence bands. This phenomenon is known as complete ionization of the charge carriers at room temperature, but at 0K, the electrons and holes freeze in their respective energy level, known as complete freeze-out.

Under thermal equilibrium conditions, the semiconductor is electrically neutral, a fundamental principle used to derive the thermal equilibrium concentration of charge carriers as a function of impurity doping concentration. Compensated semiconductors

contain both donor and acceptor impurities, and the spillover of these impurities into n-type or p-type material causes the formation of n-type ($N_d > N_a$) or p-type ($N_d < N_a$) compensated semiconductors. If both carrier concentrations are the same, the compensated semiconductor behaves like an intrinsic semiconductor.

The equilibrium concentration of charge carriers in a compensated semiconductor can be expressed as a quadratic equation.

$$n_0 = \frac{(N_d - N_a)}{2} + \sqrt{\left(\frac{(N_d - N_a)}{2}\right)^2 + n_i^2} \tag{42}$$

$$p_0 = \frac{(N_a - N_d)}{2} + \sqrt{\left(\frac{(N_a - N_d)}{2}\right)^2 + n_i^2} \tag{43}$$

7.2. Importance of Fermi Level

The equilibrium concentration of charge carriers in a semiconductor is given by equation 23 and 24. These equations can be expressed in the form of logarithmic functions as follows:

$$E_c - E_F = kT \ln\left(\frac{N_c}{n_0}\right) \tag{44}$$

$$E_F - E_V = kT ln\left(\frac{N_V}{p_0}\right) \tag{45}$$

For n-type and p-type semiconductors, $n_0 = N_d$ and $p_0 = N_a$ respectively. So that,

$$E_C - E_F = kT \ln\left(\frac{N_C}{N_d}\right) \tag{46}$$

$$E_F - E_V = kT ln\left(\frac{N_V}{N_a}\right) \tag{47}$$

For n-type semiconductors, the equilibrium concentration of electrons (n_0) is equal to the concentration of donor impurities (N_d), while for p-type semiconductors, the equilibrium concentration of holes (p_0) is equal to the concentration of acceptor impurities (N_a). The equations above demonstrate the logarithmic relationship between the distances of the band edge positions, the Fermi level, and the concentration of charge carriers. Increasing the concentration of donors or acceptors causes the Fermi level to move toward the band edges, increasing the concentration of carriers in the respective bands. In the case of compensated semiconductors, the values of N_d and N_a in Equation 45 can be replaced by $N_d - N_a$ and $N_a - N_d$, respectively. For intrinsic semiconductors, slight modifications are required for Equation 46 and 47, and they can be expressed as:

$$E_F - E_{Fi} = kT ln\left(\frac{n_0}{n_i}\right) \tag{48}$$

$$E_{Fi} - E_F = kT ln\left(\frac{p_0}{n_i}\right) \tag{49}$$

It is worth noting that the Fermi level (E_F) is situated above the intrinsic Fermi level (E_{Fi}) for n-type semiconductors and below for p-type semiconductors. The concentration of charge carriers in any semiconductor material is temperature-dependent, and temperature changes affect the position of the Fermi level in a semiconductor. As the temperature increases, carrier concentrations increase, and the Fermi level shifts towards the intrinsic Fermi level. In other words, extrinsic semiconductors exhibit behaviour at higher temperatures similar to intrinsic semiconductors.

When two electronic systems come into contact, the Fermi levels of both systems equilibrate. For instance, in the p-n junction shown in Figure 3, the energy states are filled up to
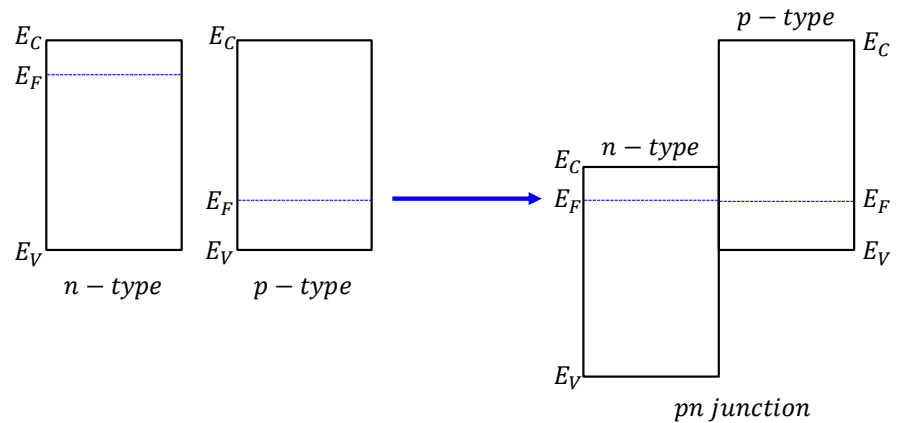
Figure 6. Energy diagram of a p-n junction before and after contact.

E_{F1} and E_{F2} in the first and second semiconductors, respectively. When these two materials come into contact, the electrons in the system occupy the lowest energy level, resulting in electron transfer from the system with a higher electrochemical potential to the one with a lower potential (or from the one with a lower work function to the one with a higher work function). This process creates a space charge layer, and it is known as Fermi-level equilibration. However, not all electron transfers across semiconductor heterojunctions are smooth, as depicted in Figure 2. Various heterojunction formulations exist, and the nature of electron transfer across each is different. If we irradiate the heterojunction in Figure 2 with a light greater than the bandgap, electrons transfer from the second system to the first (from the one with a higher work function to the one with a lower work function), and holes move in the opposite direction [16]. It is worth noting that the charge carrier transfer across the heterojunction is not smooth, as described in the situation mentioned earlier. There are more than twenty heterojunction formulations, and the nature of electron transfer differs in each formulation [17]. Furthermore, the Fermi level reaches equilibrium when a semiconductor is in direct contact with any metal [18].

Similarly, when a semiconductor material comes in contact with an electrolyte, the Fermi levels of both equilibrate, resulting in the formation of a space charge layer at the interface (see Fig. 4). This equilibration causes a change in energy levels within the semiconductor, leading to an energy difference between the surface interface and the bulk of the semiconductor. This energy difference is referred to as band bending [19-20], and the nature of band bending depends on the type of semiconductor and electrolyte used. It is important to note that the term 'band bending' refers to the interface being at a higher (in depletion and inversion layers) or lower (in accumulation layers) energy level than that of the bulk, and there is no actual bending of the energy levels between the surface and bulk. Further details on this topic will be discussed in the next section.

7.3. Electrical Double Layer at Semiconductor/Electrolyte Interfaces

Extensive literature and books have discussed the topic of the semiconductor/electrolyte interface [21-25], and the concepts presented in Norio Sato's book [26] have been adopted in the following discussion. The interface between the semiconductor and electrolyte consists of three layers: (a) a space charge layer on the semiconductor side with a thickness of 10-100 nm, (b) a compact layer at the interface with a thickness of 0.4-0.6 nm, and (c) a diffuse layer on the solution side with a thickness of 1-10 nm, as illustrated in Figure 3.
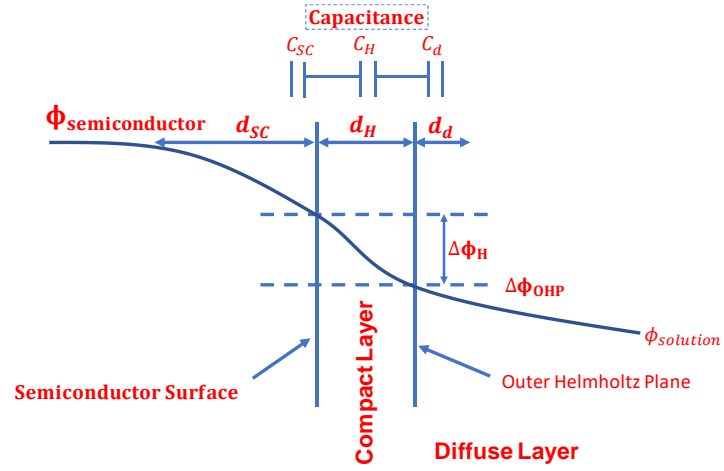
Figure 7. The electrical double layer at the semiconductor-electrolyte interface.

We can represent electroneutrality across the semiconductor/electrolyte interface using the following charges: the charge of the space charge layer as σ_{SC}, the charge of surface states as σ_{SS}, the charge of adsorbed layers present in the compact layer as σ_{ad}, and the excess ionic charge of hydrated ions in the diffuse layer as σ_S. Mathematically, this can be expressed as:

$$\sigma_{SC} + \sigma_{SS} + \sigma_{ad} + \sigma_S = 0 \tag{50}$$

This equation indicates that the sum of all charges at the interface must be zero for electroneutrality to be maintained.

The total potential across the semiconductor interface, $\Delta\phi$, can be expressed as the sum of potentials existing in the individual layers at the interface. These layers include the diffuse layer in the solution interior ($\Delta\phi_d$), the potential across the compact layer in the outer Helmholtz plane ($\Delta\phi_H$), and the potential across the interior space charge layer of the semiconductor ($\Delta\phi_{SC}$).

$$\Delta\phi = \Delta\phi_d + \Delta\phi_H + \Delta\phi_{SC} \tag{51}$$

The thickness of the space charge and diffuse layers is directly related to the total concentration of mobile charge carriers in the semiconductor, denoted as n_i, and the concentration of ions in the aqueous solution. The thickness of these respective layers is calculated using the Debye length (L_D).

$$L_D = \sqrt{\frac{\varepsilon kT}{2e^2 \sum n_i z_i^2}} \tag{52}$$

The thickness of the space charge layer and diffuse layer is directly related to the total concentration of mobile charge carriers present in the semiconductor, ni, as well as the ions in the aqueous solution, and can be calculated using the Debye length (LD). The Debye length is typically around 100 nm for semiconductors with an impurity concentration of 10^{-15} cm^{-3} and 10 nm in a 0.1 M ionic solution. In 1983, Rudiger Memming [22] derived a quantitative relationship between the thickness of the space charge layer and the Debye length, as shown in Equation 35.

$$d_{SC} = 2 \times L_d \sqrt{\left(\frac{e\delta\phi_{SC}}{kT}\right) - 1} \tag{53}$$

The total differential capacitance C at the semiconductor-electrolyte interface can be obtained by considering the equation of a series plate capacitor that comprises C_{SC}, C_H, and C_d, which represent the capacitance of the space charge layer, compact layer, and diffuse layer, respectively. Since the total capacitance of a series-connected system is determined by the smallest capacitance value, the capacitance of the semiconductor interface is approximately equal to the capacitance of the space charge layer.

$$\frac{1}{C} = \frac{1}{C_{SC}} + \frac{1}{C_H} + \frac{1}{C_d} \tag{54}$$

The total potential across the semiconductor interface can be expressed in Equation 37 regarding the Debye length.

$$\Delta\phi = E_{SC}\dot{L}_{D,SC} + E_H\dot{d}_H + E_S\dot{L}_{D,S} \tag{55}$$

If the charges of the surface states and adsorbed layers are absent (σ_{SS} and σ_{ad}), the electrostatic equation can be rewritten as follows:

$$E_{SC}\varepsilon_{SC} = E_H\varepsilon_H = E_S\varepsilon_S \tag{56}$$

Therefore, the total potential distribution across the semiconductor/electrolyte interface can be represented as:

$$\frac{\delta\Delta\phi_H}{\delta\Delta\phi_{SC}} = \frac{E_H d_H}{E_{SC} L_{D,SC}} \tag{57}$$

After substituting $E_H = {}^{E_{SC}\varepsilon_{SC}}\!/_{\varepsilon_H}$, Eq. 39 can be modified as follows:

$$\frac{\delta\Delta\phi_H}{\delta\Delta\phi_{SC}} = \frac{\varepsilon_{SC} d_H}{L_{D,SC}\,\varepsilon_H} \tag{58}$$

Similarly, the overall potential across the space charge and diffuse layers can be derived.

$$\frac{\delta\Delta\phi_d}{\delta\Delta\phi_{SC}} = \frac{L_{D,S}\,\varepsilon_{SC}}{L_{D,SC}\,\varepsilon_S} \tag{59}$$

The equations demonstrate that the potential changes primarily occur in the space charge layer while the potentials of the other two layers remain constant. This semiconductor property is known as *band edge pinning*, where the band edge potentials of the semiconductor at the interface are fixed, and hence, the potential across the compact layer is also fixed. However, the above equations assume that the surface state charge is absent. The electrostatic equation can be expressed if the surface state charge is present, as shown in Eq. 42.

$$E_H\varepsilon_H = E_{SC}\varepsilon_{SC} + \sigma_{SS} \cong \sigma_{SS} \tag{60}$$

If the value of surface state charge, σ_{SS}, is relatively high, then the potential difference across the compact layer, $\Delta\phi_H$, can be approximated as:

$$\Delta\phi_H = E_H d_H = \frac{\sigma_{SS} d_H}{\varepsilon_H} \tag{61}$$

7.3.1. Band Edge Pinning and Fermi Level Pinning

The phenomenon known as band edge pinning occurs at the interface of a semiconductor when the Fermi level lies between the bandgap and away from the surface states and band edge positions of higher density of states. During band edge pinning, the potential across the space charge and compact layers remains constant. On the other hand, Fermi level pinning occurs when the Fermi level of a semiconductor approaches the surface states or band edge positions with a higher density of states at the interface. In this case, the potential across the space charge layer remains unchanged, but a significant change in
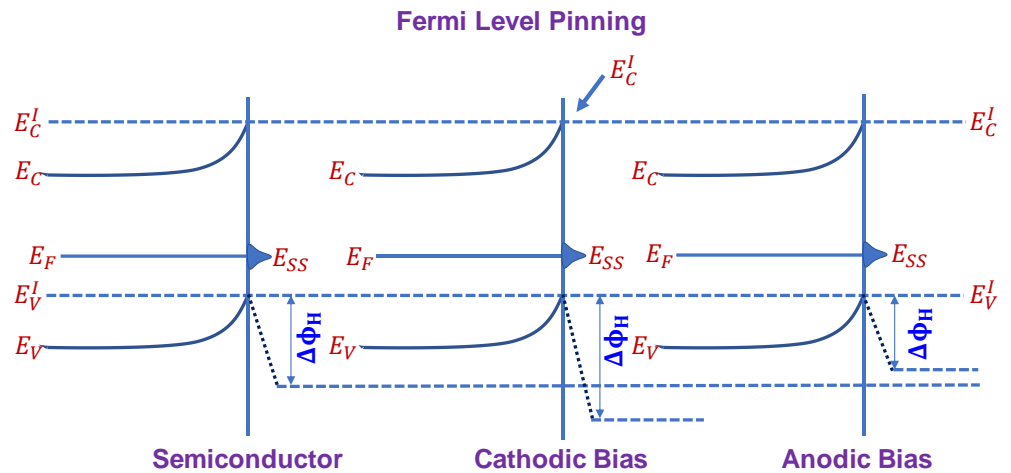
Fermi Level Pinning

Figure 8. Fermi level pinning at the semiconductor interface under different conditions.

potential occurs in the compact layer [27, 28]. When Fermi level pinning occurs, the semi-
conductor interface can behave as a metal, a phenomenon known as quasi-metalization.
Schematic representations of both phenomena are shown in Figures 4 and 5.
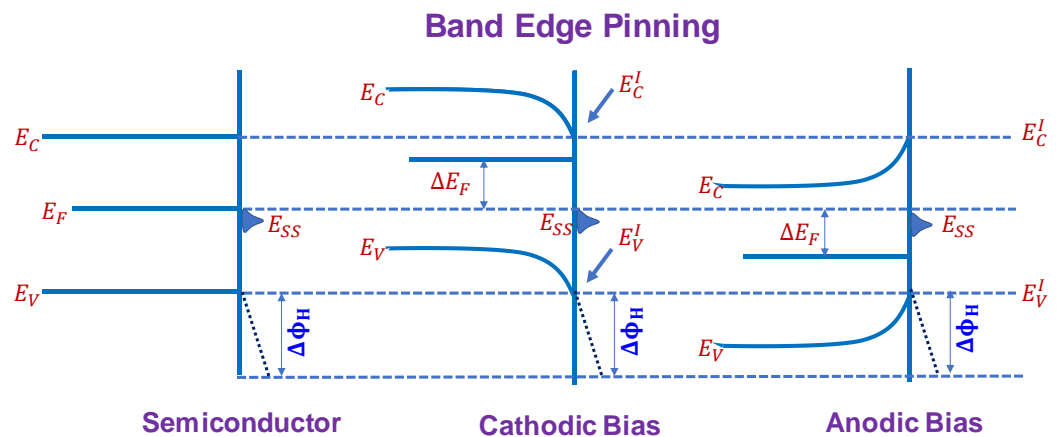
Band Edge Pinning

Figure 9. Band edge pinning of the semiconductor under different conditions.

7.3.2. Space Charge Layers

When a semiconductor comes in contact with an electrolyte solution, an interfacial
acid-base reaction generates a surface charge that significantly influences the energy levels
near the semiconductor-electrolyte interface, resulting in band bending. The point at which
the charge of the acidic and basic sites at the interface is equal is called the isoelectric point
or point of zero charges. At this point, the semiconductor exhibits flat band conditions.
When the pH is above the isoelectric point, the interface becomes negatively charged,
causing excess negative charge to repel electrons from the bulk of the semiconductor and
the interface to be at a higher energy level than the bulk, leading to upward band bending.
Conversely, a positive surface charge leads to downward band bending. The maximum
energy difference between the interface and the bulk of the semiconductor is about 0.5V,

which transports electrons and holes in opposite directions within the interfacial zone, reducing recombination. The region where band bending occurs is collectively called the space charge layer. The thickness of the space charge layer is affected by the magnitude of the interfacial charges, dielectric constant of the materials, and charge carrier concentration and is typical of the order of 100nm to 1μm. Four different types of space charge layers exist, namely, (a) accumulation layer, (b) depletion layer, (c) inversion layer, and (d) deep depletion layer (Fig. 6).

The total differential capacitance, C_{SC}, of space charge region of an intrinsic semiconductor can be represented as,

$$C_{SC} = \frac{\varepsilon}{L_D} \cosh\left(\frac{e\Delta\phi_{SC}}{2kT}\right) \tag{62}$$

Here, L_D is the Debye length (Eq. 34), n_i is the concentration of charge carrier and $\Delta\phi_{SC}$ is the potential across the space charge layer. The capacitance of the space charge layer in an n-type or p-type semiconductor can be expressed in a general form as follows:

$$C_{SC} = \frac{\varepsilon}{L_{D_{eff}}} \left(\frac{1 - \exp\left(\frac{\pm e\Delta\phi_{SC}}{kT}\right)}{\sqrt{\left|1 + \frac{\pm e\Delta\phi_{SC}}{kT} - \exp\left(\frac{\pm e\Delta\phi_{SC}}{kT}\right)\right|}} \right) \tag{63}$$

Here, $L_{D_{eff}}$ represents the effective Debye length, which is given by $\sqrt{\frac{\varepsilon kT}{2 N e^2}}$. N represents the concentration of the donor or acceptor, and the $\pm$ sign is taken as + for a p-type semiconductor and - for an n-type semiconductor. This equation provides a general expression for the capacitance of the space charge layer in a semiconductor, which can be used to derive the specific capacitances for all four types of space charge layer classifications.

7.3.2.1 Accumulation Layer

The accumulation layer is responsible for transporting the majority of charge carriers to the interface. The capacitance of the accumulation layer can be derived from the previous equation using the Boltzmann distribution. The Fermi level is assumed to be located away from the band edge positions. However, if the Fermi level is near the band edge position, Fermi level pinning occurs, and the capacitance, C_{SC}, is not dependent on the potential of the space charge layer.

$$C_{SC} = \frac{\varepsilon}{L_{D_{eff}}} \exp\left(\frac{e\Delta\phi_{SC}}{kT} - 1\right) \approx \frac{\varepsilon}{2L_{D_{eff}}} \exp\left(\frac{e\Delta\phi_{SC}}{kT}\right) \tag{64}$$

The conditions for the potential difference across the space charge layer ($\Delta\phi_{SC}$) are $|e\Delta\phi_{SC}| > 3kT$ and $\Delta\phi_{SC} < 0$ for n-type semiconductors, and $\Delta\phi_{SC} > 0$ for p-type semiconductors.

7.3.2.2 Depletion Layer

The depletion region is formed when the majority charge carriers are depleted from the semiconductor/electrolyte interface, and the minority charge carriers are transported to the interface [29]. In the capacitance equation, for an n-type semiconductor, $|e\Delta\phi_{SC}| > 3kT$ and $\Delta\phi_{SC} > 0$, while for a p-type semiconductor, $\Delta\phi_{SC} < 0$ and $|e\Delta\phi_{SC}| > 3kT$.

$$C_{SC} = \frac{\varepsilon}{2L_{D_{eff}}} \sqrt{\frac{e\Delta\phi_{SC}}{kT} - 1} \tag{65}$$

$$\frac{1}{C_{SC}^2} = \left(\frac{2L_{D,eff}}{\varepsilon}\right)^2 \left(\frac{\Delta\phi_{SC}}{kT} - 1\right) = \left(\frac{2L_{D,eff}}{\varepsilon}\right)^2 \frac{e}{kT}\left(E - E_{fb} - \frac{kT}{e}\right) \tag{66}$$
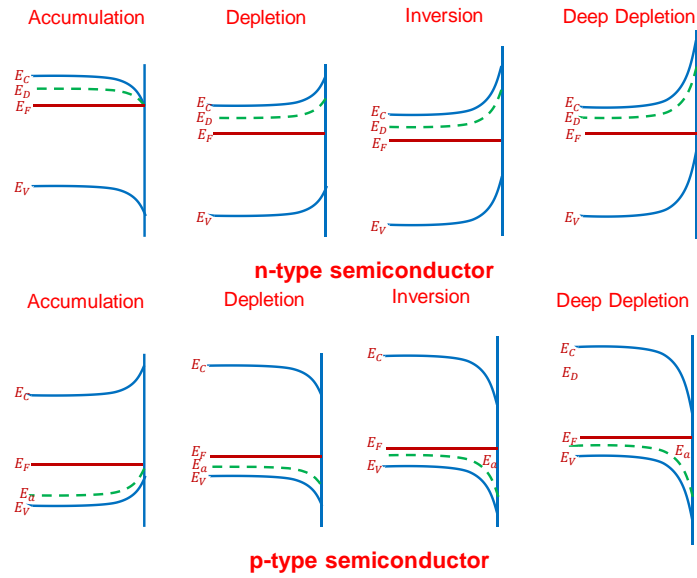
Figure 10. Different types of Space Charge Layer in an n-type and p-type Semiconductor

The equation is known as the Mott-Schottky equation, which relates the capacitance of the space charge region to the applied potential. Here, E represents the potential of the semiconductor at the interface, and E_{fb} represents the flat band potential. The Mott-Schottky plot of $\frac{1}{C_{SC}^2}$ versus E determines a semiconductor's flat band potential and effective Debye length. In the Mott-Schottky plot, the valence band edge position is obtained for n-type semiconductors, while the conduction band edge position is obtained for p-type semiconductors. The energy barrier associated with the depletion region is commonly known as the Schottky barrier.

7.3.2.3 Inversion Layer

When the Fermi level at the interface approaches the band edge position corresponding to the minority charge carriers, it can form an inversion layer, which increases the potential change of the depletion region. This inversion layer accumulation of minority charge carriers at the interface can cause a reversal in the interfacial property from n-type to p-type or p-type to n-type. Thus, this type of space charge layer is called an inversion layer. The capacitance equation for the inversion layer is similar to the accumulation layers.

$$C_{SC} = \frac{\varepsilon}{2L_{D_{min}}} \exp\left(\frac{e\Delta\phi_{SC}}{2kT}\right) \tag{67}$$

The Debye length of minority charge carriers is represented by $L_{D_{min}} = \sqrt{\frac{\varepsilon k_B T}{2n_{min}e^2}}$, where n_{min} denotes the concentration of minority charge carriers. For n-type and p-type semiconductors, $\Delta\phi_{SC} > 0$ and $\Delta\phi_{SC} < 0$, respectively. Fermi level pinning occurs in the inversion layer as the potential $\Delta\phi_{SC}$ increases, resulting in a constant band edge position and capacitance.

7.3.2.4 Deep Depletion Layer

Deep depletion is a space charge layer commonly observed in large bandgap semiconductors. It is an extension of the depletion layer and is characterized by the consumption of minority charge carriers due to faster interface reactions than carrier generation. This leads to the formation of an insulating layer at the interface. The capacitance of the deep depletion layer can be determined using the Mott-Schottky relation.

7.3.2.5　Compact Layer

Hydroxylation of the semiconductor produces acid and base sites on the surface of the semiconductor, attracting other ions to the surface and forming a compact layer at the interface of the semiconductor. This hydroxylated semiconductor surface shows a positive charge in acidic solutions and a negative charge in basic solutions. The potential across the compact layer is represented as $\Delta\phi H$.

$$\Delta\phi_H = Constant + \frac{kT}{e} \ln\left[H^+_{aq}\right] = Constant - 2.3\frac{kT}{e}(\text{pH}) \qquad (68)$$

This equation indicates the linear relationship between solution pH and the potential across the compact layer. The potential of the compact layer ($\Delta\phi_H$) is the sum of the interfacial potential ($\Delta\phi_\sigma$) resulting from the interfacial charge (σ_H) and the dipole potential ($\Delta\phi_{dipole}$) generated by the interfacial dipole.

$$\Delta\phi_H = \Delta\phi_\sigma + \Delta\phi_{dipole} \qquad (69)$$

The point at which the interfacial charge (σ_H) becomes zero is known as the point of zero charges (PZC) or isoelectric point (IEP) of a semiconductor. Equation 50 can be expressed in terms of the isoelectric point as follows:

$$\Delta\phi_H = \Delta\phi_{dipole} - 2.3\frac{kT}{e}(\text{pH} - \text{pH}_{\text{IEP}}) \qquad (70)$$

$$\Delta\phi_H = d\text{pH} \times 59 \text{ mV/pH} \qquad (71)$$

Hence, a change of one pH unit results in a potential change of 59 mV across the compact layer. By rearranging the electroneutrality equation at the interface involving the interfacial hydroxyl charge (σ_H), we get:

$$\sigma_{SC} + \sigma_{SS} + \sigma_H + \sigma_{ad} + \sigma_S = 0 \qquad (72)$$

When the semiconductor is in flat band conditions σ_{SC}=0, the equation simplifies as follows:

$$\sigma_{SS} + \sigma_H + \sigma_{ad} + \sigma_S = 0 \qquad (73)$$

For typical semiconductors, the charge of surface states (σ_{SS}) and the charge of adsorption (σ_{ad}) can be assumed to be zero or constant. In such cases, the flat band potential can be calculated as follows:

$$E_{FB} = E_{FB,IEP} - 2.3\frac{kT}{e}(pH - pH_{IEP}) \qquad (74)$$

The above equation shows that the flat band potential at the point of zero charges (PZC) or isoelectric point (IEP) is denoted by $E_{FB,IEP}$. It also indicates that the conduction band position shifts towards more negative values at a rate of 59mV/pH with an increase in the solution pH. In most cases of simple and compound semiconductors, the flat band potential changes linearly with the pH of the solution. However, there are exceptions to this trend, such as in the case of WSe$_2$, where the flat band potential is not pH-dependent but depends on the concentration of hydrated selenide ions, known as the potential-determining ion. Typically, adsorbed hydroxylated groups (hydrated protons and hydroxyl groups) are the potential-determining ion, which gives the flat band potential a linear dependence on pH. However, in the case of metal chalcogenides like metal sulphides, selenides, and tellurides, the flat band potential remains constant with a change in the pH of the solution because the concentration of hydrated chalcogenides acts as the potential-determining ion.

7.4. Semiconductor in Non-Equilibrium

G. N. Lewis and M. Randall [31] proposed that it is not coal itself but coal combustion that causes a steam engine to operate. As a general rule, changes within a system can

affect another system. To harness its processes for performing useful work, a system far
from its equilibrium state is chosen. Therefore, by harnessing the processes of a disturbed
semiconductor under equilibrium, useful energy can be generated, redox reactions can be
carried out, or electricity can be generated in solar cells.

7.4.1. Charge Carrier Recombination Mechanisms

When a semiconductor is illuminated with threshold light, it produces electrons
and holes in the conduction and valence bands, respectively, and disturbs the thermal
equilibrium. This leads to excess charge carriers present in the respective bands, which
violates Eq. 19.

$$np > n_i^2 \tag{75}$$

Here, n and p denote the nonequilibrium excess concentrations of electrons and holes.
Upon recombination, the electron and hole regain thermal equilibrium. Recombination
of charge carriers is beneficial to photocatalysts, as it prevents charge accumulation in
a particular band. In direct bandgap materials, the valence and conduction bands are
vertically aligned, resulting in a high absorption coefficient, as only the threshold photon
energy is required to excite an electron from the valence band to the conduction band. In
contrast, in indirect bandgap materials, extra energy from phonons is required in addition
to the photon energy for excitation, as the bands are not vertically aligned. The same applies
to recombination, where direct recombination is spontaneous in direct bandgap materials
but not in indirect bandgap materials, such as crystalline silicon. In such materials, the
auger recombination mechanism is predominant over radiative recombination mechanisms.
Various types of recombination processes exist depending on semiconductor properties,
which are discussed in this section [10, 32].

7.4.1.1 Direct Recombination

The radiative generation and recombination mechanism is mainly present in direct
band gap materials. In this mechanism, the generation of excitons requires the band gap
energy and emits the same amount of energy when the excitons recombine. At equilibrium
temperature, the product of the excess carrier concentration of electrons (n) and holes (p) is
equal to the intrinsic carrier concentration squared (n_i^2). Some bonds break at temperatures
above 0K, and electron-hole pairs are generated at a rate of $G_{thermal}$ or G_{th}. In other
words, the rate of recombination ($R_{thermal}$ or R_{th}) and generation are the same at thermal
equilibrium. Therefore, in thermal equilibrium situations, the recombination rate is directly
proportional to the concentration of charge carriers.

$$R_{th} = G_{th} \tag{76}$$

$$R_{th} = \beta n_0 p_0 \tag{77}$$

At nonequilibrium conditions, the equivalent equation can be expressed as follows: β
represents the proportionality constant.

$$R* = \beta np \tag{78}$$

We can write the total recombination rate as a function of the equilibrium concentrations
(n_0, p_0) and the excess carrier concentrations ($\Delta n = n - n_0, \Delta p = p - p_0$).

$$R^* = \beta np = \beta(n_0 + \Delta n)(p_0 + \Delta p) \tag{79}$$

The total generation rate of excitons can be expressed as the sum of the generation rate at
thermal equilibrium (G_{th}) and non-equilibrium conditions (G_L).

$$G = G_{th} + G_L \tag{80}$$

At steady state conditions, the rate of generation and recombination are equal.

$$G_L = R^* - G_{th} = \beta(np - n_0 p_0) = R_d \tag{81}$$

The net radiative recombination rate, denoted as R_d, can be expressed for n-type semiconductors when $\Delta n \ll n$ and $p \ll n$ as follows:

$$R_d = \beta n_0 (p - p_0) = \frac{p - p_0}{\tau_p} \tag{82}$$

The symbol τ_p represents the lifetime of minority charge carriers, specifically holes. The excess charge carrier concentration can be expressed as the product of the generation rate and the lifetime of minority charge carriers.

$$p - p_0 = G_L \tau_p \tag{83}$$

If the semiconductor has no excess charge carriers, the net recombination rate, R_d, would be zero. When the irradiation is stopped, the generation rate of charge carriers becomes zero, and the excess charge carrier concentration can be expressed as follows:

$$\frac{dp}{dt} = -\frac{p(t) - p_0}{\tau_p} \tag{84}$$

The above equation can be solved to obtain the following:

$$p(t) = p_0 + G_L \tau_p exp(-1/\tau_p) \tag{85}$$

The lifetime of minority charge carriers can be defined as the time constant at which the excess carrier concentrations decay exponentially when the generation rate of charge carriers is zero. This definition helps to understand the exact meaning of the lifetime of minority charge carriers. Similarly, for p-type semiconductors where $\Delta p \ll p$ and $n \ll p$, the recombination rate can be expressed as follows:

$$R_d = \beta p_0 (n - n_0) = \frac{n - n_0}{\tau_n} \tag{86}$$

The symbol τ_n denotes the lifetime of electrons in the semiconductor. The diffusion length of any minority carrier can be expressed in terms of the lifetime as:

$$L_n = \sqrt{D_n \tau_n} \tag{87}$$

for electrons in p-type semiconductors

$$L_p = \sqrt{D_p \tau_n} \tag{88}$$

for holes in m-type semiconductors
The symbols D_n, D_p, L_n, and L_p represent the diffusion coefficients and diffusion lengths of minority charge carriers.

7.4.1.2 Shockley-Read-Hall (SRH) Recombination

The recombination process in this type occurs through trap states (E_T) created due to lattice defects or impurity atoms. The electron trapped in the trap state attracts the hole, and recombination dissipates heat to the lattice. There are two types of trap states based on

the nature of impurities or defects - donor-type traps and acceptor-type traps.

The SRH recombination rate for an intrinsic semiconductor can be expressed as:

$$R_{SRH} = v_{th}\sigma N_T \frac{np - n_i^2}{n + p + 2n_i cosh\left(\frac{E_T - E_{Fi}}{k_B T}\right)}$$ (89)

For n-type semiconductor, the excess electron concentration is almost similar to the thermal equilibrium electron concentrations, n$\approx n_0$ and $n \gg$ p.

$$R_{SRH} = v_{th}\sigma N_T \frac{p - p_0}{1 + 2\frac{n_i}{n_0}\cosh\left(\frac{E_T - E_{Fi}}{k_B T}\right)} = c_p N_T (p - p_0) = \frac{p - p_0}{\tau_{p,SRH}}$$ (90)

The hole capture coefficient and hole lifetime in an n-type semiconductor are denoted by c_p and $\tau_{p,SRH}$, respectively, while v_{th} represents the thermal velocity. Similarly, the recombination rate in a p-type semiconductor can be written in terms of the electron capture coefficient (c_n) and electron lifetime ($\tau_{n,SRH}$).

$$R_{SRH} = v_{th}\sigma N_T \frac{p - p_0}{1 + 2\frac{n_i}{p_0}\cosh\left(\frac{E_T - E_{Fi}}{k_B T}\right)} = c_n N_T (n - n_0) = \frac{n - n_0}{\tau_{p,SRH}}$$ (91)

The lifetime of the minority charge carrier in all the above cases is inversely proportional to the density of trap states.

$$\tau_{p,SRH} = \frac{1}{c_p N_T} \; ; \; \tau_{n,SRH} = \frac{1}{c_n N_T}$$ (92)

For more detailed information on charge carrier recombination statistics of Shockley-Read-Hall Recombination can be found in the references [32-34].

7.4.1.3 Auger Recombination

Auger recombination is three particle process involves electrons, holes, and a neighbour electron or hole. Thus, carrier concentrations have a strong dependence on the Auger recombination process. In this process, the energy and momentum during the recombination process are transfers to the next electron or hole and excites to higher energy levels. The relaxation of this third carrier dissipates energy in the form of vibrational energy of the lattice. The auger recombination rate can be express as,

$$\mathbf{R}eeh = Cnn^2 p = C_n N_D^2 p$$ (93)

$$\mathbf{R}ehh = Cpnp^2 = C_p N_A^2 n$$ (94)

Where C_n and C_p are temperature-dependent proportionality constants, and R_{eeh} and R_{ehh} are the Auger recombination rates for n-type and p-type semiconductors, respectively. The Auger lifetime in n-type and p-type semiconductors can be expressed as follows:

$$R_{eeh} = \frac{1}{C_n N_d^2} \; ; R_{ehh} = \frac{1}{C_p N_A^2}$$ (95)

The Auger recombination rate is proportional to the donor or acceptor density square. Thus at higher doping levels, Auger recombination dominates over other recombination processes.

7.4.1.4 Surface Recombination

The recombination mechanisms described earlier occur within the volume of a semiconductor. However, surface recombination processes become more dominant than bulk recombination processes in semiconductors with high purity levels. This is because surface trap states are generated within the band gap due to dangling bonds at the semiconductor surfaces. The rate of surface recombination for both n-type and p-type semiconductors can be expressed as:

$$R_{sn} = v_{th}\sigma_p N_{ST}(p_s - p_0) \tag{96}$$

$$R_{sp} = v_{th}\sigma_n N_{ST}(n_s - n_0) \tag{97}$$

The capture cross-section of holes and electrons is denoted by σ_p and σ_n, respectively. N_{ST} represents the density of surface traps. The concentrations of holes and electrons at the surface are denoted by p_s and n_s, while p_0 and n_0 represent the thermal equilibrium concentrations of holes and electrons.

7.4.2. Concept of Quasi-Fermi Level

Under thermal equilibrium, when a semiconductor is exposed to light with energy more significant than its bandgap, electrons are excited from the valence band to the conduction band, producing excitons in both bands. In the case of an n-type semiconductor, this irradiation has little effect on the concentration of conduction band electrons (the majority charge carrier) but increases the concentration of holes (the minority charge carrier) in the valence band. Similarly, in p-type semiconductors, the irradiation enhances the concentration of electrons (the minority charge carrier) and has minimal impact on the concentration of holes (the majority charge carrier). Therefore, irradiating a semiconductor generally increases the concentration of minority charge carriers.

$$n^* = n + \Delta n \tag{98}$$

$$p^* = p + \Delta p \tag{99}$$

The concentration of electrons and holes in the dark and under irradiation are represented by n, p, n^*, and p^*, respectively. Δn^* and Δp^* indicate the increase in the concentration of charge carriers after irradiation. During photoexcitation, charge carriers equilibrate with phonons in their respective bands. Irradiation splits the Fermi level into two: the quasi-Fermi level of electrons and the quasi-Fermi level of holes. The electrochemical potential of electrons and holes in the photo-stationary state is referred to as the quasi-Fermi level of electrons ($E_F^{n^*}$) and the quasi-Fermi level of holes ($E_F^{p^*}$), respectively. In the absence of irradiation (under thermal equilibrium), the quasi-Fermi and Fermi levels of the semiconductor are the same. Under photoexcitation conditions, the quasi-Fermi level of electrons is situated above the Fermi level, while the quasi-Fermi level of holes is below the Fermi level (see Figure 7).

$$E_F^* = E_C - kT\,ln\left(\frac{N_C}{n^*}\right) = E_F + kT\,ln(n) + \Delta n \cdot n \tag{100}$$

$$E_F^{p^*} = E_V + kT\ln\left(\frac{N_V}{p^*}\right) = E_F - kT\ln p + \Delta p p^* \tag{101}$$

In an n-type semiconductor, where $n \gg p$ and $n \gg \Delta n^*$, the quasi-Fermi level of electrons is nearly equal to the Fermi level, while the quasi-Fermi level of holes ($p < \Delta p^*$) is located much lower than the Fermi level. Generally, under photoexcitation conditions, the quasi-Fermi level of the majority charge carriers is either very close to or approximately the same as the Fermi level.
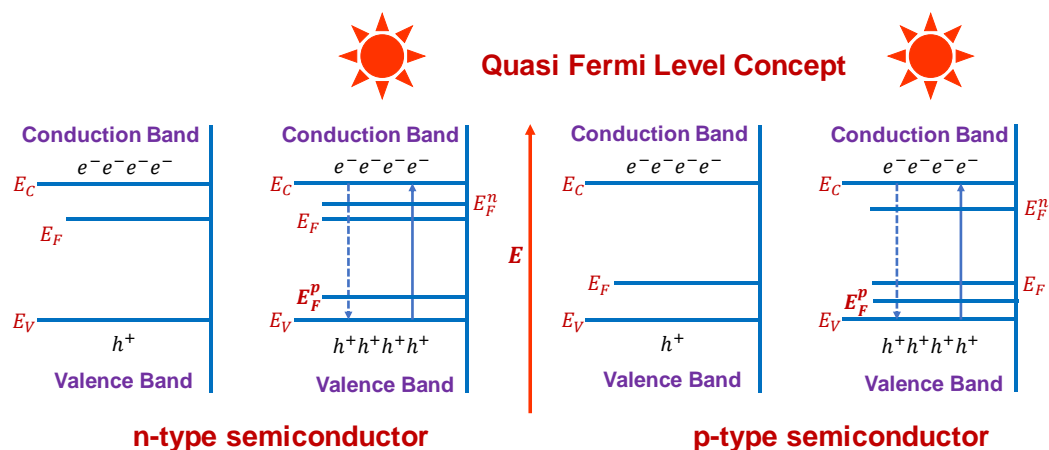
Figure 11. Splitting of Fermi level to quasi-Fermi levels in the presence of irradiation and quasi-Fermi level formation in n- and p-type semiconductors.

Under equilibrium conditions, the Fermi levels of the redox species and the semiconductor are balanced, resulting in no electron transfer and no reaction without irradiation. If electron transfer could occur between the semiconductor and redox species, the Fermi level of the semiconductor should be above that of the redox species. This criterion is achieved when the semiconductor is irradiated with threshold light. The requirement for a reduction reaction is that the quasi-Fermi level of the electrons should be higher than that of the redox species, allowing the electrons from the conduction band to flow to the oxidant species. Similarly, the quasi-Fermi level position of the hole must be lower than that of the reductant species for the reduction reaction to occur.

$$E_F^* n > E_{F_{redox}} \tag{102}$$

$$E_F^{p^*} < E_{F_{redox}} \tag{103}$$

Let us use the water-splitting reaction as an example to illustrate the concepts above. When an n-type semiconductor is immersed in water, the Fermi levels of both species reach equilibrium. As a result, the semiconductor does not possess the sufficient potential to either reduce or oxidize the redox species, making the reaction thermodynamically infeasible under dark conditions. However, in the presence of irradiation, the Fermi level splits into two quasi-Fermi levels and aligns above and below the redox potential of water. As a result, the necessary prerequisites for reduction and oxidation are satisfied, and water undergoes a redox reaction under these circumstances (refer to Fig. 8).

$$E_F^{n^*} > E_{F_{\left(\frac{H_2O}{H_2}\right)}} \tag{104}$$

$$E_F^{p^*} < E_{F_{\left(\frac{O_2}{H_2O}\right)}} \tag{105}$$

This is the reason why the water-splitting reaction or any other photocatalytically driven reaction is thermodynamically impossible in the absence of any irradiation or field.

7.4.3. Photo-potential

As we discussed earlier, the flat band condition of the semiconductor results in the recombination of charge carriers, while the space charge layer formed at the interface
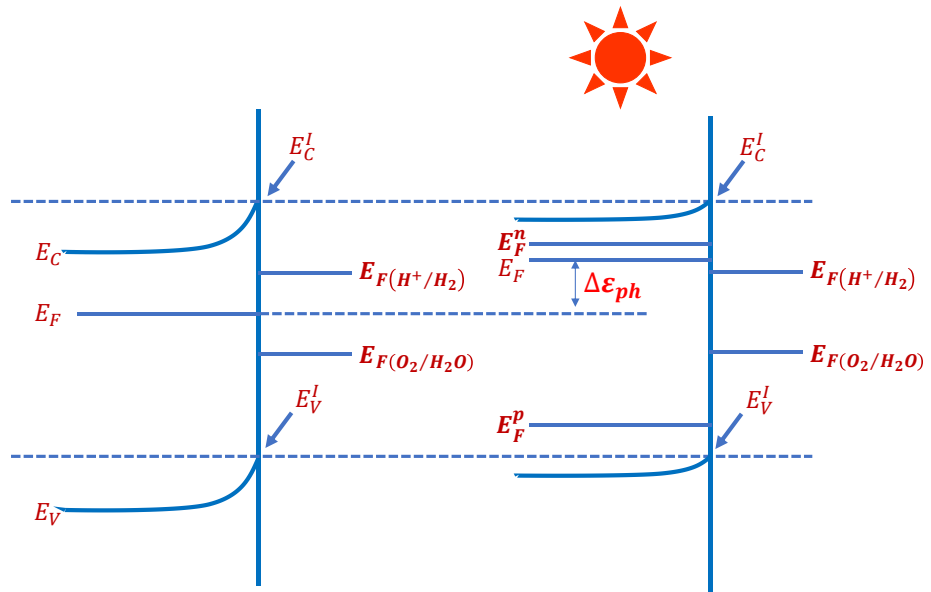
Figure 12. Band characteristics of the semiconductor in presence and absence of illumination concerning water redox potential.

separates the charge carriers by transporting them in opposite directions. This separation of charge carriers induces an inverse potential in the semiconductor, which reduces the potential across the space charge layer. This decrease in potential slows down the migration of charges in the opposite direction. The photo-excitation-induced inverse potential in the space charge layer is the photo potential.

$$\Delta E_{ph} = -\Delta \epsilon_{ph} \tag{106}$$

During photoexcitation, when the band bends upwards, the Fermi level of the semiconductor moves up by an energy of $\Delta \varepsilon_{ph}$, while it moves down when the band bends downwards. Hence, the maximum photo-potential (ΔE_{ph}^0) of a semiconductor can be determined as the difference between the potential of the semiconductor in the dark (E) and its flat band potential (E_{fb}) during irradiation, where the band bending disappears.

$$|\Delta E_{ph}| \leq \Delta E_{ph}^0 = |E - E_{fb}| \tag{107}$$

If no interfacial chemical reaction is present, the photo potential value of a semiconductor with a high impurity concentration can be approximated from the charge carrier concentration (Fig. 9).
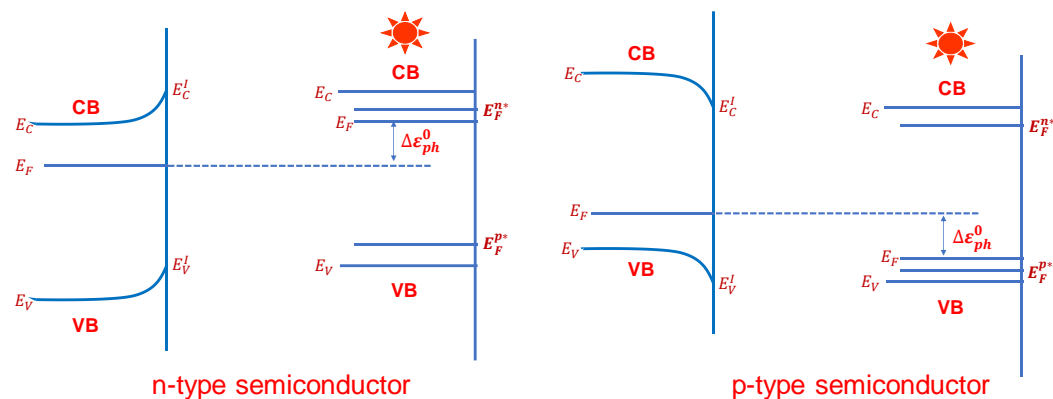
Figure 13. Generation of photopotential under illumination in n-type & p-type semiconductors.

8. Basic Postulates and Principles

The design of a photoelectrode for CO_2 reduction involves various interrelated factors, each playing a specific role in the overall process. These factors include the characteristics of light irradiation, light penetration into the semiconductor, absorption of photons, the generation, separation and transportation of charge carriers to the interface, and thermodynamic and kinetic factors of the interface reactions, competing reactions, and overall photoelectrode stability. The physical and chemical characteristics of the material, including particle size, surface area, pore size, active sites on the surface, and morphology, have a noticeable impact on the CO_2 reduction process. As these factors are interrelated, their correlations are complicated. More than just focusing on the material's inherent properties is required for a viable process. Therefore, efficient optimization of all physical, chemical, and electrochemical parameters is necessary to select and design new materials for CO_2 reduction.

8.1. Photon Management

The excitation of charge carriers is the critical process in PEC cells, achieved through constant-intensity light irradiation of a specific wavelength. Changes in light intensity can significantly affect subsequent processes. Controlling the surface morphology of the photoelectrode is crucial to enhance light absorption. It is essential to understand that the absorption coefficient relies on both intrinsic material properties and the characteristics of the incident light.

Semiconductors do not absorb photons with energy lower than the band gap energy (Eg), while those with higher energy are absorbed. However, some high-energy photons can travel significantly within the semiconductor before absorption. The light intensity decreases exponentially as it travels through the semiconductor, with the rate of decay defined by the absorption coefficient or absorptivity (α). The absorption coefficient is proportional to the extinction coefficient (κ), which is the square root of the complex part of the dielectric constant. The inverse of the absorption coefficient, known as the penetration depth or skin depth (δ), is the distance over which the light intensity falls to $1/e$ of its original value in the semiconductor. The penetration depth is roughly proportional to the inverse of the square root of the dielectric constant and can be used to predict how far the light will penetrate the semiconductor. [260,261].

The frequency and semiconductor properties determine the value of the skin depth, and it represents the distance to which light can penetrate a semiconductor. For example, Fe_2O_3 has a skin depth of 118nm at 550nm, Si has a skin depth of 680nm at 510nm, and

CdTe has a skin depth of 106nm at 550nm [262]. To achieve uniform excitation within the space charge layer, the penetration depth of the incident light should be within the thickness range of the layer. By doing this, charge carrier recombination can be reduced, and better migration of charge carriers into the interface can be achieved. To minimize the recombination rate, it is essential to ensure that the bulk diffusion length is greater than the width of the space charge layer, which makes recombination via surface states negligible, resulting in no diffusion current flowing towards the interface [263]. The wavelength of the incident radiation is a critical factor that affects the penetration depth, and hence, monochromatic radiation is encouraged for CO_2 reduction to ensure precise control over the penetration depth. Therefore, when selecting the appropriate wavelength of incident radiation for any photon-assisted reaction, the penetration depth should be factored in, and the selection should not be random.

8.2. Bandgap, Photovoltage and Band Edge Positions

Designing the morphology of the photoelectrode to capture the maximum amount of incident light is crucial for efficient solar fuel generation. Roughening the surface of the photoelectrode can increase light trapping by scattering the light horizontally, thus promoting a higher degree of light distribution (Fig. 4). The flat surface of the photo-electrode is generally avoided since it increases direct reflection [264]. The particle size is also important in the solar fuel generation process, where smaller particle size provides a larger surface area-to-volume ratio. A higher surface area is essential for promoting surface reactions, and it is better in small particles than in larger ones. However, nanoscale particles may experience hindrances in carrier transportation to the surface interface, leading to rapid exciton recombination due to the low potential drop and electric field across the space charge region [263]. This, in turn, leads to increased electron-hole recombination and reduced advantages from the higher interfacial surface area. The surface and interfacial electron-hole recombination can be reduced by surface treatments that remove surface defects. The decrease in particle size increases the material's band gap due to the modification in the band edge positions resulting from quantum confinement [262,265]. On the other hand, the nanoscale particles are better reducing/oxidizing agents than the bulk semiconductor. However, the increased bandgap shifts the absorption properties into the blue region of the spectrum, reducing the absorption of visible light.

8.3. Morphology and Textural Parameters

Designing the morphology of the photoelectrode to capture the maximum amount of incident light is crucial for efficient solar fuel generation. Roughening the surface of the photoelectrode can increase light trapping by scattering the light horizontally, thus promoting a higher degree of light distribution (Fig. 4). The flat surface of the photoelectrode is generally avoided since it increases direct reflection [264]. The particle size is also crucial in solar fuel generation, where smaller particles provide a larger surface area-to-volume ratio. A higher surface area is essential for promoting surface reactions, and it is better in small particles than in larger ones. However, nanoscale particles may experience hindrances in carrier transportation to the surface interface, leading to rapid exciton recombination due to the low potential drop and electric field across the space charge region [263]. This, in turn, leads to increased electron-hole recombination and reduced advantages from the higher interfacial surface area. The surface and interfacial electron-hole recombination can be reduced by surface treatments that remove surface defects. The decrease in particle size increases the material's band gap due to the modification in the band edge positions resulting from quantum confinement [262,265]. On the other hand, the nanoscale particles are better reducing/oxidizing agents than the bulk semiconductor. However, the increased bandgap shifts the absorption properties into the blue region of the spectrum, reducing the absorption of visible light.

The rate of water splitting reaction is highly influenced by the surface area of the photoelectrode or cocatalyst, as it facilitates the transfer of charges across the interfaces.

Water-splitting reactions can occur at lower current densities when the surface area increases. Along with the surface area, the active sites in the photoelectrode or cocatalyst are crucial for capturing water on their surface lattices, further enhancing the reaction rate.

The light absorption cross-section of a photoelectrode is increased due to scattering and internal reflection within the porous layer. The smaller penetration depth in a porous photoelectrode produces minority charge carriers near the semiconductor-electrolyte interface, reducing the light-induced recombination of excitons. For instance, n-type GaP with a polished surface has a penetration depth of approximately 10 μm at 2.4 eV , larger than the hole diffusion length. Therefore, the recombination over charge transfer across the interface takes place. However, porous GaP (shown in Fig.5) allows light absorption within the porous layer, creating minority charge carriers near the interface and increasing the quantum efficiency to unity in the presence of bandgap photon energy [266,267].

8.4. Stability

The primary challenge in the photoelectrochemical cell is the vulnerability of the photoelectrode to degradation under reaction conditions. A thorough comprehension of the photo-corrosion mechanism is essential to identify the most suitable material for reaction conditions. Therefore, material selection is critical, and an independent examination is necessary to determine the appropriate measures to stabilise the photoelectrode. This analysis will help determine the optimal material for prolonged stability of the photoelectrode under reaction conditions [268].

The decomposition of photocathode and photoanode in the photoelectrochemical cell is initiated by the conduction band electrons and valence band holes, respectively. The energy of these electrons and holes is determined by the quasi-Fermi level of the photoelectrode under illumination. The position of the decomposition Fermi levels relative to the quasi-Fermi levels reflects the thermodynamic stability of the photoelectrode. Based on this understanding, the stability of a photoelectrode can be classified into four different categories [133].

When the decomposition Fermi level of a photoelectrode lies outside the bandgap, it is referred to as a stable photoelectrode. Conversely, if the level lies inside the bandgap, it is an unstable photoelectrode. The free energy difference between the band edges and the decomposition Fermi levels determines the extent of anodic and cathodic decomposition. It is ideal to have a stable photoelectrode, but no semiconductor is entirely stable against photodecomposition. Most photoelectrode materials belong to the last two categories, with some semiconductors decomposing entirely under light irradiation, as illustrated in (6b).

Geirscher has provided equations for the photoelectrode decomposition process in different scenarios. In a photocathodic reaction, a photoelectrode (MX) reacts with a solvated electron (e-) and a solvent to produce a metal ion (M) and a solvated anion ($X_{solv}{}^{Z-}$). On the other hand, in a photoanodic reaction, a photoelectrode (MX) reacts with a solvated hole (h^+) and a solvent to produce a solvated cation ($M_{solv}{}^{z+}$) and an anion (X). When holes are present on the surface, they weaken the bonding between adjacent atoms in the surface lattice, making them more susceptible to reacting with the nucleophilic reactants in the electrolyte. The extent of bond weakening depends on the localisation of wave functions, and sites like kink sites, lattice defects, and dislocations on the surface are predominantly responsible for the "transitorial hole capturing process." The interaction of these sites with the electron-donating atoms or molecules from the electrolyte causes further localisation of the hole by forming a new bond. Similarly, the localisation of electrons in the antibonding states weakens the bond with electrophilic reactants in the electrolyte, stabilising the reduced state and allowing the decomposition to proceed spontaneously.

The kinetics of a reaction is the primary determining factor for photodecomposition, as shown in Fig. 6, which presents the thermodynamic aspects of photo corrosion. The photodecomposition of the photoelectrode depends mainly on the surface kinetics of the specific surface redox reaction involved. Even in harsh conditions where thermodynamics predicts instability, the photoelectrode may remain somewhat stable, thanks to the

role of kinetics in preventing photodecomposition. The kink sites on the surface step site are responsible for the formation and decomposition of any crystals, where an atom has nearly half the binding energy compared to the same atom in the crystal's bulk. The shielding of the kink site using inhibitors slows down the photodecomposition rate. Since the photodecomposition reaction involves a series of reactions, the rate-determining step favouring the formation of the most active intermediates plays a critical role. The activation energy of the rate-determining step controls the overall rate of photodecomposition. The thermodynamic decomposition potential of the overall reaction does not provide information on the energetics of the reaction steps, and generating high-energy intermediates is considered the rate-determining step. Therefore, the redox potential corresponding to the rate-determining step is a better indicator of the photodecomposition reaction. The intermediate steps involved in the photodecomposition process depend on the surface composition and the nature of redox reactions at the interface and vary significantly with each photoelectrode. Consequently, numerous factors determine how photodecomposition begins and how fast it proceeds; no general principles can predict them. Equations 3 and 4 illustrate the generalised indication of a compound with kink sites (MX) and the successive association of the surface with the holes and ligands [129].

To prevent photodecomposition, photogenerated minority scavengers can be employed, which are typically one-electron reactions that proceed faster than photodecomposition reactions with no kinetic complications. However, these scavengers cannot be used for water-splitting reactions because the solvent is oxidized or reduced. The kinetics of water splitting impose certain restrictions on its progression, which make it capable of protecting the photoelectrode only under specific conditions where the thermodynamic potential falls far below the potential required for photodecomposition. Like photodecomposition reactions, water-splitting reactions are complicated and involve intermediate steps.

9. Surface Engineering

The technique of surface engineering is a useful tool to adjust the transport properties of charge carriers and design new semiconductor materials [292-297]. However, this section aims to focus on the problems associated with surface engineering techniques rather than their current state of development. Extensive research has been conducted in this area, and readers are encouraged to refer to the following sources [293-297]. Initially, the application of doped semiconductors in solar energy conversion was intended to increase the photon-absorption cross-section of the photoactive materials and the photoactivity. While surface engineering techniques can enhance the photoactivity towards thermodynamically favourable reactions such as pollutant degradation, this does not necessarily apply to all other solar energy utilization processes. It should also be noted that the current surface techniques do not solve the problems in water splitting or other thermodynamically unfavourable reactions such as the photoreduction of carbon dioxide [298-300].

Additionally, the phrase 'increases photoactivity' is still not widely established. Most studies on this topic only focus on thermodynamic controls over the reaction rather than the kinetics. It's important to remember that even if a reaction is thermodynamically favorable, it may not proceed well if the kinetics are slow. This is precisely the situation in photoelectrochemical water splitting, and thus, we need to focus on controlling both the thermodynamic and kinetic aspects of the reaction to make further improvements [301]. Revisiting this approach could potentially change the current paradigm.

9.1. Doped Materials

Doping is a technique in which impurities are intentionally introduced into a semiconductor matrix to modify its electrical properties. The primary use of doping was in the electronics industry to regulate carrier generation and transport. With this technique, new electronic materials like solid-state photomultiplier or resonant tunnelling transistors were developed by directly incorporating impurities into the semiconductor bulk. Another dop-

ing method involves electronic interaction between dopants and the semiconductor surface lattice. Doping can also help to fine-tune the light absorption properties of semiconductors.

Suppose we take an example of a photoelectrode, such as titanium dioxide, which can split water. In the previous section, we learned that a photovoltage of approximately 1.8V is required for efficient water splitting, which means the band gap should be over 2eV. Photovoltage refers to the potential difference between two quasi-Fermi levels located near the conduction and valence bands. When a dopant is introduced into the surface layer, it creates an intermediate state above the valence band, acting as a HOMO level, shown in Figure 9. Electrons are excited from this HOMO level to the conduction band, requiring less energy than in an undoped system. However, the oxidation potential of the undoped system is stronger than the doped one. As a result, the photovoltage generated in a doped system is less than in an undoped system due to the shift of the valence band quasi-Fermi level to a less positive value. Changes in the Fermi level in the semiconductor result in a difference in band bending at the interface with the electrolyte compared to the undoped system. [304]

Doping in a photoelectrode's surface space charge layer leads to interfacial changes that can be explained by the effect of the dopant's optimal concentration. Adding the right amount of dopant decreases the depletion region to the semiconductor's photon penetration depth, allowing for a uniform generation of charge carriers in the space charge layer. This reduces the recombination rate and enhances the charge transfer to the interface. However, if the dopant concentration is too high, the depletion layer width decreases beyond the photon penetration depth, producing fewer charge carriers in that region and, ultimately, at the interface. Excessive dopant concentration increases the recombination of charge carriers in the bulk region within photon penetration depth or acts as a recombination centre [304].

The charge density present within a doped semiconductor is critical in determining its interaction with the electrolyte. Any changes in the potential of the doped semiconductor in the electrolyte can significantly affect its kinetic stability. The doping process decreases the electrostatic repulsion between the particles, causing doped semiconductor colloids suspended in the electrolyte solution less stable. The surface chemical groups mainly affect the material's stability since the doping process modifies the surface chemistry. The decrease in electrostatic potential due to doping indicates the dominance of the van der Waals force, which can cause the particles to coagulate or precipitate [305, 306].

The figure in Fig.11 depicts the changes in the electrostatic potential distribution of an n-doped semiconductor-oxide-electrolyte system concerning the dopant concentration. As we know, the oxide layer behaves as a capacitor and is charge-free. The figure illustrates the difference in the surface potential at the oxide-electrolyte interface with doping. Screening effects significantly impact the potential distribution inside the semiconductor, whereas it only has a relatively small effect on the potential distribution in the electrolyte. This is because surface groups responsible for charge regulation interact directly with the electrolyte [307].

The only factor responsible for enhancing the water-splitting reaction or hydrogen production is the amplification in the carrier concentration at the interface, which reduces the recombination of electrons and holes. However, this increase is not significant, as it does not consider the dynamic effects at the interface. A thorough experimental study is necessary to gain further insight into the interfacial band energetics of doped semiconductors and their impact on the system's stability.

9.2. Hetero junction

A heterojunction photoelectrode is necessary to provide the required photovoltage for water splitting. It also expands the range of semiconductors that can be used since some do not have appropriate band positions to exceed the water redox potentials. Using heterojunction photoelectrode is advantageous because the electric field generated at the interface of two semiconductors can move the charge carriers in opposite directions. The literature covers different aspects and applications of heterojunction semiconductors as a

photoelectrode. To be considered a champion material for PEC water splitting, a material must have appreciable absorption characteristics, adequate band alignment concerning water redox potentials, faster reaction kinetics, and prolonged stability. Even though heterojunction photoelectrode meets the thermodynamic requirements of water splitting, the reaction rate increase is marginal and is only due to the slight reduction in the charge carrier recombination rate.

Let us examine how a heterojunction meets each of the four characteristics of a champion material for PEC water splitting. Heterojunctions do considerably enhance light absorption, but they also affect the inherent potential of the charge carriers due to charge carrier transport between the semiconductors. The oxidation/reduction potential of the semiconductors influences the movement of holes and electrons, and water oxidation occurs in a semiconductor with a lower oxidation potential, while water reduction occurs in a semiconductor with a lower reduction potential. As a result, the increased light absorption advantage may not be fully realised in the heterostructure.

In photocatalytic or photo electrocatalytic processes, the band alignment of semiconductors in heterojunctions is classified into four types: Type I, Type II, Type III, and conventional p-n junctions. However, directly using these theories to interpret the nature of electron transfer across the heterojunction is not reasonable. Instead, we need to adopt an approach based on the electron affinity and the work function of individual semiconductors. For example, Ag_2O/TiO_2 belongs to Type II heterojunction, and the band positions of Ag_2O are above that of TiO_2. Therefore, we might expect electron transfer from Ag_2O to TiO_2 and hole transfer from TiO_2 to Ag_2O after equilibrium. However, this is not the case as the built-in electric field is not continuous in the heterojunction, leading to increased recombination of charge carriers at the interface when illuminated. This results in lower efficiency than individual semiconductor systems, and the system becomes active in visible light, not UV. Further details on the construction of heterojunction interfaces are covered in earlier literature.

In addition to the thermodynamic factors, there are kinetic factors not adequately addressed by heterojunction photoelectrodes, such as the charge carrier mobility in two semiconductor systems and the surface kinetics aspects. As a result, the water-splitting reaction is not significantly enhanced by heterojunction photoelectrodes unless these kinetic issues are addressed effectively. The stability of the material and the interface is another critical aspect that has not been thoroughly explored in the literature.

When designing a photoelectrode for PEC cells, it is important to consider the interactions at three different interfaces: the photoelectrode/metal contact, the heterojunction interface between the two semiconductors, and the heterojunction photoelectrode/electrolyte interface. Detailed studies on each interface are necessary to understand the transfer of charge carriers within the heterojunction photoelectrode. However, there is currently no published research on the behaviour of these three interfaces in the presence of both an electric and photon field or a photoelectric field. In addition, various other issues, depicted in Figure 13, must be considered [321].

In order to effectively design a heterojunction photoelectrode for water splitting, it is essential to consider several issues related to the optical and electric properties of the individual semiconductors used. This includes ensuring that they meet the necessary criteria for the desired application. Additionally, it is necessary to understand the nature of the electrostatic fields that develop at the heterojunction interfaces and how defects in the parent semiconductors may affect this. Another important consideration is whether the interface formed during the heterojunction formation is thermodynamically stable. Finally, controlling the lattice mismatches at the interface is critical for achieving optimal performance. These issues are depicted in Figure 13 and must be addressed to effectively interpret the nature of carrier transfer within the heterojunction photoelectrode.

Remember that the built-in electric field and band bending will only be symmetrical when the doping levels in the individual semiconductors are similar. Therefore, much research is necessary to create a highly active heterojunction photoelectrode. If this research

is not conducted, the interface will obstruct the carrier flow, resulting in the instability of the interface. These issues indicate significant room for improvement in designing a heterojunction photoelectrode for overall water splitting.

9.3. Plasmonincs

The primary purpose of adding plasmonic metals to a photoelectrode is to enhance its optical absorption in the visible region and decrease the activation barrier for water-splitting [323-325]. However, this has not been thoroughly investigated in the literature. Among plasmonic metals, plasmonic gold nanoparticles are the most researched photoelectrode systems due to their resistance to oxidation [326]. The mechanism of plasmon-enhanced PEC water splitting is not yet fully understood, and there are conflicting opinions on the mode of oxygen evolution on the plasmonic metal surface. Proposed mechanisms, such as direct electron transfer (DET) and plasmonic resonant energy transfer (PRET), do not offer a detailed explanation of the various phenomena occurring at the plasmonic interface [327-329]. A better understanding of these aspects is necessary to design improved semiconductor plasmonic interfaces. A recent study (Fig. 14) suggested that plasmon-generated holes at the semiconductor/plasmonic metal interface are responsible for and identified as the reaction site for water oxidation [330].

Numerous studies have compared the operation of plasmonic semiconductors to the dye-sensitization mechanism. However, such a comparison may not be relevant because the potential dependence of the photocurrent in a dye-sensitized photoelectrode is similar to that of the bare dye molecule. In contrast, in a plasmonic semiconductor, it is similar to that of the bare photoelectrode. This implies that the local surface plasmon resonance (LSPR) decays as UV light rather than hot electrons, and the efficiency of the overall process is determined by the distribution of electric field and potential across the space charge layer. Moreover, upconversion at the plasmonic interface is possible due to energy pooling between particles with similar physical properties, such as size, shape, and separation distance, which must be below the plasmon wavelength. Therefore, the efficiency of hot electron injection is profoundly influenced by the particle shape, size, and concentration of the plasmonic metal on the photoelectrode surface.

The hot electron injection efficiency (HEIE) is influenced by the type of support semiconductor used and the interface quality formed in the photoelectrode. Surface defects can increase the Schottky barrier height between the plasmonic metal and the semiconductor, resulting in a lower HEIE. Thus, appropriate surface treatment should be carried out before depositing the plasmonic metal onto the photoelectrode surface to avoid such issues.

It is crucial to validate the proposed mechanisms of plasmon-mediated PEC water splitting experimentally. The interface's theoretical design typically only considers the work functions of the photoelectrode and the plasmonic metal, but in reality, contact with water can alter the work function of both materials [333]. As a result, these changes must be considered when interpreting the mechanism of water oxidation on plasmonic photoelectrodes. The behaviour of the interface may differ from that of a theoretical design for the photoelectrode/plasmonic interface.

9.4. The Co-Catalyst

Bunsho Ohtani article

10. Conclusion and Perspectives

This section may be divided by subheadings. It should provide a concise and precise description of the experimental results, their interpretation as well as the experimental conclusions that can be drawn.

Bulleted lists look like this:

- First bullet;
- Second bullet;

- Third bullet. 1234

    Numbered lists can be added as follows: 1235

1. First item; 1236
2. Second item; 1237
3. Third item. 1238

    The text continues here. 1239

10.1. Figures, Tables and Schemes 1240

All figures and tables should be cited in the main text as Figure 14, Table 1, etc. 1241

Figure 14. This is a figure. Schemes follow the same formatting. If there are multiple panels, they should be listed as: (**a**) Description of what is contained in the first panel. (**b**) Description of what is contained in the second panel. Figures should be placed in the main text near to the first time they are cited. A caption on a single line should be centered.

Table 1. This is a table caption. Tables should be placed in the main text near to the first time they are cited.

Title 1	Title 2	Title 3
Entry 1	Data	Data
Entry 2	Data	Data [1]

[1] Tables may have a footer.

The text continues here (Figure 15 and Table 2). 1242

Figure 15. This is a wide figure.

Table 2. This is a wide table.

Title 1	Title 2	Title 3	Title 4
Entry 1 *	Data Data Data	Data Data Data	Data Data Data
Entry 2	Data Data Data	Data Data Data	Data Data Data
Entry 3	Data Data Data	Data Data Data	Data Data Data
Entry 4	Data Data Data	Data Data Data	Data Data Data

* Tables may have a footer.

Text.

Text.

10.2. Formatting of Mathematical Components

This is the example 1 of equation:

$$a = 1,\tag{108}$$

the text following an equation need not be a new paragraph. Please punctuate equations as regular text.

This is the example 2 of equation:

$$a = b + c + d + e + f + g + h + i + j + k + l + m + n + o + p + q + r + s + t + u + v + w + x + y + z \quad (109)$$

Please punctuate equations as regular text. Theorem-type environments (including propositions, lemmas, corollaries etc.) can be formatted as follows:

Theorem 1. *Example text of a theorem.*

The text continues here. Proofs must be formatted as follows:

Proof of Theorem 1. Text of the proof. Note that the phrase "of Theorem 1" is optional if it is clear which theorem is being referred to. □

The text continues here.

11. Discussion

Authors should discuss the results and how they can be interpreted from the perspective of previous studies and of the working hypotheses. The findings and their implications should be discussed in the broadest context possible. Future research directions may also be highlighted.

12. Conclusions

This section is not mandatory, but can be added to the manuscript if the discussion is unusually long or complex.

13. Patents

This section is not mandatory, but may be added if there are patents resulting from the work reported in this manuscript.

Institutional Review Board Statement: In this section, you should add the Institutional Review Board Statement and approval number, if relevant to your study. You might choose to exclude this statement if the study did not require ethical approval. Please note that the Editorial Office might ask you for further information. Please add "The study was conducted in accordance with the Declaration of Helsinki, and approved by the Institutional Review Board (or Ethics Committee) of NAME OF INSTITUTE (protocol code XXX and date of approval)." for studies involving humans. OR "The animal study protocol was approved by the Institutional Review Board (or Ethics Committee) of NAME OF INSTITUTE (protocol code XXX and date of approval)." for studies involving animals. OR "Ethical review and approval were waived for this study due to REASON (please provide a detailed justification)." OR "Not applicable" for studies not involving humans or animals.

Informed Consent Statement: Any research article describing a study involving humans should contain this statement. Please add "Informed consent was obtained from all subjects involved in the study." OR "Patient consent was waived due to REASON (please provide a detailed justification)." OR "Not applicable" for studies not involving humans. You might also choose to exclude this statement if the study did not involve humans.

Written informed consent for publication must be obtained from participating patients who can
be identified (including by the patients themselves). Please state "Written informed consent has been
obtained from the patient(s) to publish this paper" if applicable.

Data Availability Statement: We encourage all authors of articles published in MDPI journals to
share their research data. In this section, please provide details regarding where data supporting
reported results can be found, including links to publicly archived datasets analyzed or generated
during the study. Where no new data were created, or where data is unavailable due to privacy or
ethical re-strictions, a statement is still required. Suggested Data Availability Statements are available
in section "MDPI Research Data Policies" at https://www.mdpi.com/ethics.

Acknowledgments: In this section you can acknowledge any support given which is not covered by
the author contribution or funding sections. This may include administrative and technical support,
or donations in kind (e.g., materials used for experiments).

Conflicts of Interest: Declare conflicts of interest or state "The authors declare no conflict of interest."
Authors must identify and declare any personal circumstances or interest that may be perceived as
inappropriately influencing the representation or interpretation of reported research results. Any role
of the funders in the design of the study; in the collection, analyses or interpretation of data; in the
writing of the manuscript; or in the decision to publish the results must be declared in this section. If
there is no role, please state "The funders had no role in the design of the study; in the collection,
analyses, or interpretation of data; in the writing of the manuscript; or in the decision to publish
the results".

Sample Availability: Samples of the compounds ... are available from the authors.

Abbreviations

The following abbreviations are used in this manuscript:

MDPI	Multidisciplinary Digital Publishing Institute
DOAJ	Directory of open access journals
TLA	Three letter acronym
LD	Linear dichroism

Appendix A

Appendix A.1

The appendix is an optional section that can contain details and data supplemental to
the main text—for example, explanations of experimental details that would disrupt the
flow of the main text but nonetheless remain crucial to understanding and reproducing
the research shown; figures of replicates for experiments of which representative data are
shown in the main text can be added here if brief, or as Supplementary Data. Mathematical
proofs of results not central to the paper can be added as an appendix.

Table A1. This is a table caption.

Title 1	Title 2	Title 3
Entry 1	Data	Data
Entry 2	Data	Data

Appendix B

All appendix sections must be cited in the main text. In the appendices, Figures, Tables,
etc. should be labeled, starting with "A"—e.g., Figure A1, Figure A2, etc.

References

1. Aresta, M.; Dibenedetto, A., The CO$_2$ Revolution. In *The Carbon Dioxide Revolution: Challenges and Perspectives for a Global Society*; Springer International Publishing: Cham, 2021; pp. 219–228. https://doi.org/10.1007/978-3-030-59061-1_12.
2. Aresta, M.; Dibenedetto, A. Carbon Recycling Through CO$_2$-Conversion for Stepping Toward a Cyclic-C Economy. A Perspective. *Frontiers in Energy Research* **2020**, *8*, 159. https://doi.org/10.3389/fenrg.2020.00159.

3. Aresta, M.; Dibenedetto, A.; Angelini, A. The changing paradigm in CO_2 utilization. *Journal of CO_2 Utilization* **2013**, *3-4*, 65–73. https://doi.org/10.1016/j.jcou.2013.08.001.

4. Dibenedetto, A.; Marcolongo, D.M.; Aresta, M. Conversion of CO_2 to Fuels. In *Reference Module in Earth Systems and Environmental Sciences*; Elsevier, 2022. https://doi.org/10.1016/B978-0-323-90386-8.00026-7.

5. Marcolongo, D.M.; Aresta, M.; Dibenedetto, A. Chapter Nine - Stepping toward the carbon circular economy (CCE): Integration of solar chemistry and biosystems for an effective CO_2 conversion into added value chemicals and fuels. In *Recent Highlights I*; Hubbard, C.D.; van Eldik, R., Eds.; Academic Press, 2021; Vol. 78, *Advances in Inorganic Chemistry*, pp. 289–351. https://doi.org/10.1016/bs.adioch.2021.04.003.